

The long-wavelength thermal emission of the Pluto-Charon system from *Herschel* ^{*} observations. Evidence for emissivity effects.

E. Lellouch¹, P. Santos-Sanz², S. Fornasier¹, T. Lim³, J. Stansberry⁴, E. Vilenius^{5,6}, Cs. Kiss⁷, T. Müller⁶, G. Marton⁶, S. Protopapa⁸, P. Panuzzo⁹, and R. Moreno¹

¹ LESIA, Observatoire de Paris, PSL Research University, CNRS, Sorbonne Universités, UPMC Univ. Paris 06, Univ. Paris Diderot, Sorbonne Paris Cité, 5 place Jules Janssen, 92195 Meudon, France
e-mail: emmanuel.lellouch@obspm.fr

² Instituto de Astrofísica de Andalucía-CSIC, Glorieta de la Astronomía s/n, 18008-Granada, Spain.

³ European Space Astronomy Centre (ESAC), P.O. Box 78, E-28691 Villanueva de la Cañada, Madrid, Spain

⁴ Space Telescope Science Institute, 3700 San Martin Drive, Baltimore, MD 21218 USA

⁵ Max-Planck-Institut für Sonnensystemforschung, Justus-von-Liebig-Weg 3, 37077 Göttingen, Germany

⁶ Max-Planck-Institut für Extraterrestrische Physik, Giessenbachstraße, 85748 Garching, Germany

⁷ Konkoly Observatory of the Hungarian Academy of Sciences, H-1121 Budapest, Konkoly Thege Miklós t 15-17, Hungary

⁸ Department of Astronomy, University of Maryland, College Park, MD 20742, USA

⁹ GEPI, Observatoire de Paris, PSL Research University, CNRS, Univ. Paris Diderot, Sorbonne Paris Cité, 5 Place Jules Janssen, 92195 Meudon, France

Received, November 2, 2015; Revised, December 19, 2015

ABSTRACT

Thermal observations of the Pluto-Charon system acquired by the *Herschel* Space Observatory in February 2012 are presented. They consist of photometric measurements with the PACS and SPIRE instruments (nine visits to the Pluto system each), covering six wavelengths from 70 to 500 μm altogether. The thermal light curve of Pluto-Charon is observed in all filters, albeit more marginally at 160 and especially 500 μm . Putting these data into the context of older ISO, *Spitzer* and ground-based observations indicates that the brightness temperature (T_B) of the system (rescaled to a common heliocentric distance) drastically decreases with increasing wavelength, from ~ 53 K at 20 μm to ~ 35 K at 500 μm , and perhaps even less at longer wavelengths. Considering a variety of diurnal and/or seasonal thermophysical models, we show that T_B values of 35 K are lower than any expected temperature for the dayside surface or subsurface of Pluto and Charon, implying a low surface emissivity. Based on multiterrain modeling, we infer a spectral emissivity that decreases steadily from 1 at 20–25 μm to ~ 0.7 at 500 μm . This kind of behavior is usually not observed in asteroids (when proper allowance is made for subsurface sounding), but is found in several icy surfaces of the solar system. We tentatively identify that a combination of a strong dielectric constant and a considerable surface material transparency (typical penetration depth ~ 1 cm) is responsible for the effect. Our results have implications for the interpretation of the temperature measurements by REX/*New Horizons* at 4.2 cm wavelength.

Key words. Kuiper belt objects: individual: Pluto, Charon. Planets and satellites: surfaces. Methods: observational. Techniques: photometric.

1. Introduction

The *New Horizons* flyby of the Pluto system on July 14, 2015 revealed Pluto and Charon as planetary worlds (Stern et al., 2015). Pluto appears to display an unexpected variety of terrain morphologies, suggesting a complex history of surface activity. These include icy plains with evidence for glacier-like flows of ice and polygonal ice patterns, mountain ridges several kilometers high, and dark, cratered, ancient terrains, where irradiation of surface ices (N_2 , CH_4 , CO) and/or atmospheric production of organic tholins falling to the surface may be responsible for the dark red color. While the identification of the processes shaping this rich geology is just beginning, it already seems clear that Pluto's surface appearance is to a large extent sculpted by interactions between its mobile volatile ices, evolving N_2 -dominated atmosphere, and surface bedrock. Mars-like

seasonal cycles must be at work, in which volatile N_2 (and the secondary species CH_4 and CO) are shared between atmospheric and surface ice reservoirs through sublimation/condensation exchanges and volatile migration. These processes are related to the temperature distribution across Pluto's surface, which reflects the balance between insolation, thermal radiation, thermal conduction, and latent heat exchanges, and depends on important parameters such as albedo, emissivity, and thermal inertia (see, e.g., Hansen & Paige, 1996; Young, 2012). At Charon, where no atmosphere has yet been detected, such resurfacing processes are less obvious, although the distinctly red color of Charon's north polar region may be related to seasonal cold trapping of volatiles in that region, followed by energetic radiation (Stern et al., 2015).

Temperature measurements on an icy surface are possible from the temperature-dependent position and shape of near-IR absorption bands (e.g., Quirico & Schmitt, 1997; Tryka et al., 1994, 1995; Grundy et al., 1999; Grundy, Schmitt & Quirico, 2002). This diagnostic is to be used by *New Horizons*/Ralph

^{*} *Herschel* is an ESA space observatory with science instruments provided by European-led Principal Investigator consortia and with important participation from NASA.

(Reuters et al., 2008), for example, for the $N_2(2-0)$ ice band at $2.15 \mu\text{m}$. The only other method for determining surface temperatures is thermal radiometry. Thermal measurements (in general spatially unresolved) of the Pluto system at a variety of wavelengths (from ~ 20 to $1400 \mu\text{m}$) have been acquired using IRAS, ISO, and *Spitzer*, and a number of ground-based mm/submm facilities. In particular, the ISO and *Spitzer* measurements clearly detected the Pluto+Charon thermal light curve that is associated with the albedo contrasts on Pluto and the diurnal variability of insolation. These measurements have provided the first determination of the thermal inertia of Pluto and Charon, and some constraints on their emissivity behavior over $20\text{--}160 \mu\text{m}$ (Lellouch et al., 2000a, 2011).

The operation of *Herschel* (Pilbratt et al., 2010) in 2009–2013 offered an opportunity to extend the study toward longer wavelengths ($70\text{--}500 \mu\text{m}$), bridging the gap with the sub-mm/mm measurements. Combined with previous *Spitzer* data, these measurements permit us to refine our estimates of Pluto’s and Charon’s thermal inertia, and determine the long-wavelength behavior of the system’s emission. Following an initial assessment of the data (Lellouch et al., 2013a), we present a detailed report of these observations and their modeling. The *Herschel* $70\text{-}\mu\text{m}$ data that are described below have already been used to derive limits on the amount of dust in the Pluto–Charon system (Marton et al., 2015).

2. Herschel observations

We obtained thermal photometry of the Pluto system with the two imaging photometers of *Herschel*, PACS (Photoconductor Array Camera and Spectrometer; Poglitsch et al. (2010)) and SPIRE (Spectral and Photometric Imaging Receiver; Griffin et al. (2010)), covering altogether six wavelengths. The SPIRE instrument observes a $4' \times 8'$ field simultaneously in three bolometer arrays at $250 \mu\text{m}$, $350 \mu\text{m}$, and $500 \mu\text{m}$, with respective pixel sizes of $6''$, $10''$, and $13''$. PACS can operate in three filters, centered at $70 \mu\text{m}$ (“blue”), $100 \mu\text{m}$ (“green”), and $160 \mu\text{m}$ (“red”). However, as it includes two detector arrays (64×32 pixels of $3.2'' \times 3.2''$ for blue/green and 32×16 pixels of $6.4'' \times 6.4''$ for red, each of them covering a FOV of $3.5' \times 1.75'$), only two filters out of three ($70 / 160 \mu\text{m}$ or $100 / 160 \mu\text{m}$) are observed in parallel.

For both instruments, the beam size ($17''\text{--}35''$ FWHM for SPIRE and $5''\text{--}11''$ FWHM for PACS, depending on filter) encompassed the entire $\sim 1''$ -wide Pluto system, thus including thermal emission from Pluto and Charon (with a negligible contribution from the other four moons). All data were acquired over three weeks in late February to mid-March 2012, under the OT2_ellouc_2 program (“Pluto’s seasonal evolution and surface thermal properties”). We acquired nine observations of the Pluto system with each instrument. They were timed to sample equally-spaced subobserver longitudes, so as to provide a multi-band thermal light curve. In practice, consecutive visits to Pluto were scheduled with a time separation of ~ 17 hours, equivalent to $\sim 40^\circ$ longitude. The SPIRE observations occurred over Feb. 29 – Mar. 6, 2012, while the PACS data were taken on Mar. 14–19, 2012. Pluto’s heliocentric distance at that time was $r_h = 32.19$ AU, the subsolar latitude was $\beta = 47.0^\circ$, and the phase angle was 1.6° .

We acquired the SPIRE observations in the small-map mode. The telescope was scanned across the sky at $30''/\text{sec}$, in two nearly orthogonal (84.8° angle) scan paths, uniformly covering an area of $5' \times 5'$. Each SPIRE visit to Pluto amounted to 1421 sec, corresponding to ten repetitions of the scanning pattern.

We used the mini scan map mode for PACS, which has been demonstrated to be more sensitive than the point-source (chop-nod) mode (Müller et al., 2010)¹. For each filter combination ($70 / 160 \mu\text{m}$ or $100 / 160 \mu\text{m}$), we acquired data consecutively in two scanning directions (termed “A” and “B”), with 70° and 110° angles with respect to the detector array and individual integration times of 286 sec per scan, i.e., 1144 sec (4 repetitions) per PACS visit. Observational details are given in Table 1, where the A-B scanning sequences are indicated by consecutive Obs. ID numbers.

Far-infrared photometry can often be plagued by confusion noise, i.e., spatial variations in the sky emission at scales comparable to the PSF. The confusion noise is typically $\sim 5\text{--}7$ mJy/beam in the SPIRE bands (Nguyen et al., 2010) and lower in the PACS bands, but Pluto’s 2012 position in star-crowded regions of Sagittarius not far from Galactic center made sky background levels a priori more severe. Estimates of confusion levels at proposal stage indicated that even though the March 2012 epoch was most favorable in this respect (and selected for that reason), it would be subject to confusion noise at the ~ 5 and ~ 20 mJy in the PACS $100 \mu\text{m}$ and $160 \mu\text{m}$ beams, respectively, i.e., a non-negligible fraction of the expected fluxes from Pluto (~ 400 and 300 mJy, respectively). However, the proper motion of Pluto offered the possibility to observe the target several times against different sky backgrounds, permitting us to subtract the sky contribution. The efficiency of this “follow-on” (a.k.a. second-visit) approach has been demonstrated by the detection of numerous TNOs at the mJy level by *Spitzer* and *Herschel* (e.g., Stansberry et al., 2008; Santos-Sanz et al., 2012). For the technique to work, the proper motion between two visits should be significantly larger than the PSF size, but remain small enough that at the second visit, the object still falls within the high-coverage area of the map from the first visit. In practice, these conditions are best met for proper motions of $30''\text{--}50''$ for PACS observations and $72''\text{--}150''$ for SPIRE. In our observing sequence, the proper motion of Pluto between two consecutive visits (~ 17 hour separation) was of $55\text{--}35$ arcsec, almost entirely in the RA direction (and decreasing with time as Pluto approached stationarity on April 10, 2012). Thus, for PACS observations, each visit to Pluto could be used as second epoch measurement for the preceding and/or following visit (17 hours before or after). For SPIRE, we often used more distant visits (i.e., 34 or 51 hours before or after a given observation) for the second epoch, as difference maps between two contiguous visits would result in the positive and negative Pluto images in the differential map to partially overlap at $500 \mu\text{m}$.

3. Data reduction

PACS: Data reduction was initially performed within the *Herschel* Interactive Processing Environment (HIPE; Ott, 2010), version 12, using its default FM7 calibration scheme and an optimum script for “bright” sources. Each PACS visit to Pluto provides two images (A and B scans) at $70 \mu\text{m}$ and $100 \mu\text{m}$, and four images at $160 \mu\text{m}$. For the green ($100 \mu\text{m}$) and red ($160 \mu\text{m}$) data, each image of a given visit was analyzed in combination with the corresponding image of the previous (“before”) or successive (“after”) visit to Pluto. The exception to this was, of course, for the first (resp. last) visit to Pluto for which only the “after” (resp. “before”) image could be used. This permitted us

¹ See also AOT Release Note: PACS Photometer Point/Compact Source Mode 2010, PICS-ME-TN-036, Version 2.0, custodian Th. Müller (PACS Photometer Point/Compact Source Mode, 2010).

Table 1. Summary of observations

Obs. ID	Instrument/Mode	Filter	Start Time (2012-)	T _{obs} (sec.)	Δ ^a	Longitude ^b	Flux ^c (mJy)
1342239786	SPIREPhoto	250/350/500	02-29 20:08:23	1421	32.649	28.0	179.9±2.7 / 107.9±2.9 / 58.4±3.5
1342239900	SPIREPhoto	250/350/500	03-01 13:04:38	1421	32.638	347.5	176.8±2.0 / 105.8±3.0 / 56.0±3.5
1342239979	SPIREPhoto	250/350/500	03-02 06:30:10	1421	32.627	306.8	174.8±3.0 / 106.2±2.9 / 57.7±3.5
1342240025	SPIREPhoto	250/350/500	03-02 22:44:11	1421	32.617	268.8	175.5±2.9 / 104.9±3.1 / 58.6±3.5
1342241087	SPIREPhoto	250/350/500	03-03 16:21:25	1421	32.606	227.4	171.9±2.8 / 106.0±3.1 / 59.4±3.6
1342241158	SPIREPhoto	250/350/500	03-04 09:17:02	1421	32.596	187.6	170.7±2.9 / 106.2±3.0 / 56.5±3.5
1342240277	SPIREPhoto	250/350/500	03-05 02:18:31	1421	32.585	147.6	174.9±2.9 / 106.3±3.0 / 56.5±3.5
1342240315	SPIREPhoto	250/350/500	03-05 19:12:47	1421	32.574	107.9	184.9±2.9 / 111.9±3.0 / 59.8±3.5
1342240318	SPIREPhoto	250/350/500	03-06 11:44:14	1421	32.563	69.1	186.9±3.0 / 116.6±2.9 / 63.9±3.5
1342241381-2	PACSPhoto	70/160	03-14 03:02:01	2x286	32.442	358.7	321.9±8.6 / / 331.0±10.1
1342241383-4	PACSPhoto	100/160	03-14 03:13:39	2x286	32.442	358.2	/ 393.3±4.0 / 331.0±10.1
1342241418-9	PACSPhoto	70/160	03-14 19:54:46	2x286	32.431	319.1	316.5±2.7 / / 317.3±20.9
1342241420-1	PACSPhoto	100/160	03-14 20:06:24	2x286	32.431	318.6	/ 406.1±7.9 / 317.3±20.9
1342241471-2	PACSPhoto	70/160	03-15 12:58:39	2x286	32.419	279.0	312.2±7.3 / / 313.3±20.0
1342241473-4	PACSPhoto	100/160	03-15 13:10:17	2x286	32.419	278.6	/380.4±13.4/ 313.3±20.0
1342241509-0	PACSPhoto	70/160	03-16 06:33:59	2x286	32.407	237.6	295.0±7.1 / / 314.8±13.6
1342241511-2	PACSPhoto	100/160	03-16 06:45:37	2x286	32.407	237.2	/ 377.2±3.6 / 314.8±13.6
1342241620-1	PACSPhoto	70/160	03-17 00:10:12	2x286	32.395	196.3	299.8±3.5 / / 309.9±10.5
1342241622-3	PACSPhoto	100/160	03-17 00:21:50	2x286	32.395	195.8	/ 371.1±7.1 / 309.9±10.5
1342241655-6	PACSPhoto	70/160	03-17 17:31:54	2x286	32.384	155.5	311.5±4.5 / / 307.5±16.6
1342241657-8	PACSPhoto	100/160	03-17 17:43:32	2x286	32.384	155.1	/ 379.3±9.3 / 307.5±16.6
1342241699-0	PACSPhoto	70/160	03-18 11:04:14	2x286	32.372	114.3	342.1±2.8 / / 329.7±12.6
1342241701-2	PACSPhoto	100/160	03-18 11:15:52	2x286	32.372	113.9	/ 418.3±2.9 / 329.7±12.6
1342241865-6	PACSPhoto	70/160	03-19 04:42:46	2x286	32.360	72.9	347.6±12.4 / / 338.7±25.7
1342241867-8	PACSPhoto	100/160	03-19 04:54:24	2x286	32.360	72.4	/ 426.9±6.2 / 338.7±25.7
1342241928-9	PACSPhoto	70/160	03-19 20:44:31	2x286	32.349	35.2	349.1±4.4 / / 353.0±18.5
1342241930-1	PACSPhoto	100/160	03-19 20:56:09	2x286	32.349	34.8	/ 413.9±3.9 / 353.0±18.5

^a Observer-centric distance^b Subobserver east longitude at mid-point. We adopt the same orbital conventions as, e.g., Buie, Tholen, & Wasserman (1997) and Lellouch et al. (2011). Zero longitude on Pluto is the sub-Charon point. The subobserver point longitude decreases with time.^c Color-corrected fluxes. PACS 160- μ m fluxes are given for the average over four consecutive Obs. IDs (see text)

to generate two background maps, which were then subtracted from the individual image, providing a cleaner map suited for photometry. Standard aperture photometry on the resulting difference image was performed with our own IRAF/DAOPHOT-based routines via a curve-of-growth approach to determine the optimum synthetic aperture and a Monte-Carlo method of 200 fictitious source implantations to estimate error bars (see Santos-Sanz et al. (2012) and Kiss et al. (2014) for details). The method thus provided in general (i.e., except for the first and last visit, for which two times fewer values were obtained) four (in the green) or eight (in the red) individual values of the flux (f_i , error bar σ_i) per visit. The sky subtraction did not bring any noticeable improvement for blue (70- μ m) data, which have the least background contamination. Therefore, we simply performed aperture photometry on the original A and B images, providing two sets of values per visit. The optimum aperture radii were found to be 5.5", 7.0", and 10.5" in the blue, green, and red bands, respectively, i.e., close to the PSF FWHM at the corresponding wavelengths. For each filter and visit, the 2 to 8 (1 to 4 for first and last visit) individually-determined fluxes were (error-bar weighted) averaged. To be conservative, we took the final error on the average flux to be $\max(\text{std}(f_i), 1/\sqrt{\sum \frac{1}{\sigma_i^2}})$, where $\text{std}(f_i)$ is the standard deviation of the individual fluxes. Minor color corrections were finally applied, by dividing the averaged fluxes and their error bars by factors of 0.983 (70- μ m), 0.982 (100- μ m), and 1.000 (160- μ m), appropri-

ate (to within ± 0.01) for respective color temperatures of 47 K, 45 K, and 43 K. The final flux values are gathered in Table 1. Additional systematic calibration uncertainties (5 % of the measured flux), which do not affect the light curves, are not included in Table 1.

SPIRE: SPIRE data were first processed using HIPE, version 10, including de-stripping routines that minimize background differences between data acquired at different epochs and that properly correct the signal timeline. Then, maps were produced using the standard naive map-making, projecting the data of each band on the same World Coordinate System (WCS) and applying cross-correlation routines between two epochs to correct for astrometry offsets. Finally, for each Pluto visit, several difference maps were computed at each band by subtracting, from the map under consideration, maps taken at other epochs, separated by $\sim \pm 17$, ± 34 and/or ± 51 hours (also depending on the considered filter). Photometry on these difference maps was then performed with a two-dimensional circular Gaussian aperture with a fixed filter-dependent FWHM (PSF fitting), following the method described in Fornasier et al. (2013). The derived flux was then corrected by the instrument pixellization factors, i.e., dividing by 0.951, 0.931, and 0.902 for 250, 350, and 500 μ m, respectively. Finally, color corrections were estimated by convolving a blackbody emission at 35–40 K, the approximate system brightness temperature at the SPIRE wavelengths, with the instrument spectral response profiles. These multiplicative color correction factors were found to be 0.974, 0.976, and 0.957

at 250, 350, and 500 μm , and applied to the individual Pluto-Charon fluxes. The final system flux for each visit was then computed as the weighted mean of the individual fluxes based on the various differential maps (in a few cases after rejecting some outliers). Final fluxes with all corrections included are gathered in Table 1. Similar to PACS, the errors include the uncertainties provided by the Gaussian fitting algorithm, but do not account for absolute calibration uncertainties, which are estimated to be 7% of the measured flux. The final PACS and SPIRE fluxes were converted into system brightness temperatures (T_B) by assuming a 1185 km radius for Pluto and 604 km for Charon. The Charon radius is based on stellar occultation (Sicardy et al., 2006). The adopted Pluto radius is close to the best guess value from Lellouch et al. (2015), 1184 km. These values match initial reports from *New Horizons* (606 ± 3 km and 1187 ± 4 km; Stern et al., 2015). Results would be insignificantly sensitive to further changes of the radii by a few kilometers. The adopted value for Pluto’s radius updates the value that was used in previous modeling of the ISO and *Spitzer* data (1170 km). The effect is negligible at 24 μm (a ~ 0.1 K decrease in the T_B) but not entirely so at 500 μm (~ 0.5 K decrease).

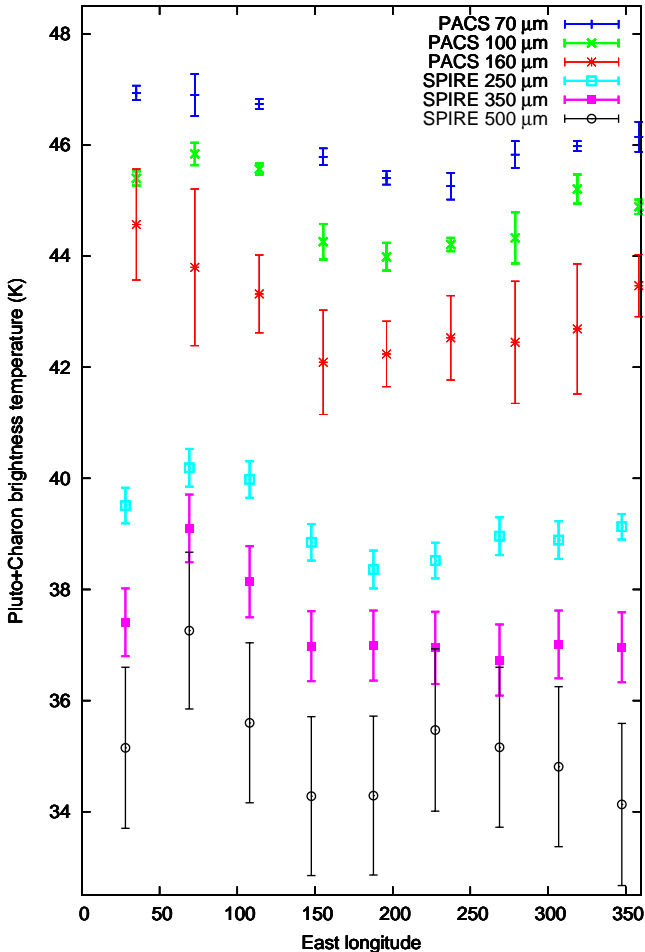


Fig. 1. Pluto-Charon thermal light curves in the six filters observed with PACS and SPIRE.

4. Modeling

4.1. Qualitative analysis

Brightness temperatures of the Pluto-Charon system over 70–500 μm as a function of rotational phase are shown in Fig. 1. Immediately apparent in the figure is that: (i) the mean brightness temperature (T_B) of the system decreases steadily with increasing wavelength from ~ 46.5 K at 70 μm to ~ 35 K at 500 μm ; and (ii) the thermal light curve is detected at all wavelengths, albeit somewhat marginally at 160 μm and especially 500 μm , given the higher error bars of these data. At 70 and 160 μm , the data are of much higher quality than was possible from *Spitzer* (see Fig. 2 from Lellouch et al. (2011); hereafter Paper I). All data are consistent with maximum flux near an east longitude $L = 60$ –80 and minimum flux near $L = 200$ –220. More quantitatively, sinusoidal fits to the data yield flux maxima at $L = 57\pm 5$, 50 ± 8 , 42 ± 22 , 57 ± 10 , 76 ± 17 , and 70 ± 60 for 70, 100, 160, 250, 350, and 500- μm data. Thus, within measurements uncertainties, all light curves appear in phase (in particular, there is excellent phase agreement between the 70 μm , 100 μm and 250 μm data). Out-of-phase light curves at the longest wavelengths had been envisaged in Paper I.

In Fig. 2, the *Herschel* measured brightness temperatures are plotted as a function of wavelength and put into the broader context of most previous thermal measurements of the Pluto-Charon system. These measurements include (i) ISOPHOT 60, 100, 150, and 200 μm photometry, taken mostly in Feb.-March 1997 (five to eight visits to Pluto; Lellouch et al. (2000a)); (ii) *Spitzer*/MIPS 23.68, 71.42, and 156 μm photometry and *Spitzer*/IRS low-resolution spectroscopy over 20–37 μm recorded in August–September 2004 (eight visits to Pluto each; Paper I); (iii) additional *Spitzer*/MIPS data at 23.68 and 71.42 μm taken in April 2007 (12 visits; see Fig. 13 of Paper I), and unpublished 156 μm data from October 2008 (12 visits); and (iv) a number of ground-based measurements at mm/sub-mm wavelengths from IRAM, JCMT, and SMA (Altenhoff et al., 1988; Stern, Weintraub & Festou, 1993; Jewitt, 1994; Lellouch et al., 2000b; Gurwell, Butler & Moullet, 2011). We emphasize that the SMA data separate Pluto from Charon, and we report the Pluto-only T_B from 2005 and 2010. In Figure 2, *Spitzer*/MIPS and IRS data from 2004 at eight longitudes are plotted individually. We reinterpolate, to the same eight longitudes, the *Herschel* (70, 100, 160, 250, 350, and 500 μm), *Spitzer* 71.42 μm from 2007, and ISO 60 and 100 μm data, all of which clearly show light curves. For data in which we did not discern (or attempt to detect) a light curve, i.e., ISO 150 and 250 μm , *Spitzer* 156 μm from October 2008, and all of the ground-based data, we simply plotted the mean T_B averaged over the available measurements. All of the ISO, *Spitzer*, and *Herschel* T_B in Fig. 2 make consistent use of the above Pluto and Charon radii. In contrast, mm/sub-mm T_B simply use published values, because of the difficulty in tracking down the originally used radii. All these thermal measurements span 25 years (1986–2012), a period over which Pluto’s heliocentric distance (r_h) and subsolar latitude (β) varied from 29.7 AU to 32.2 AU and from -4° to $+47^\circ$, respectively. While the effect of a change in the subsolar latitude cannot be accounted for without a detailed model, the effect of varying r_h is handled by rescaling the measured T_B by $1/\sqrt{r_h}$ to the epoch of the *Spitzer* 2004 data ($r_h = 30.847$ AU).

Fig. 2 illustrates a number of important features. (i) The difficult-to-explain Pluto “fading” witnessed by *Spitzer*, i.e., the decrease by ~ 2 K of the 71 μm T_B (and by ~ 0.5 K at 24 μm) over 2004–2007 (Paper I) is not confirmed in the *Herschel* data, which indicates 70- μm T_B in good agreement with the *Spitzer*

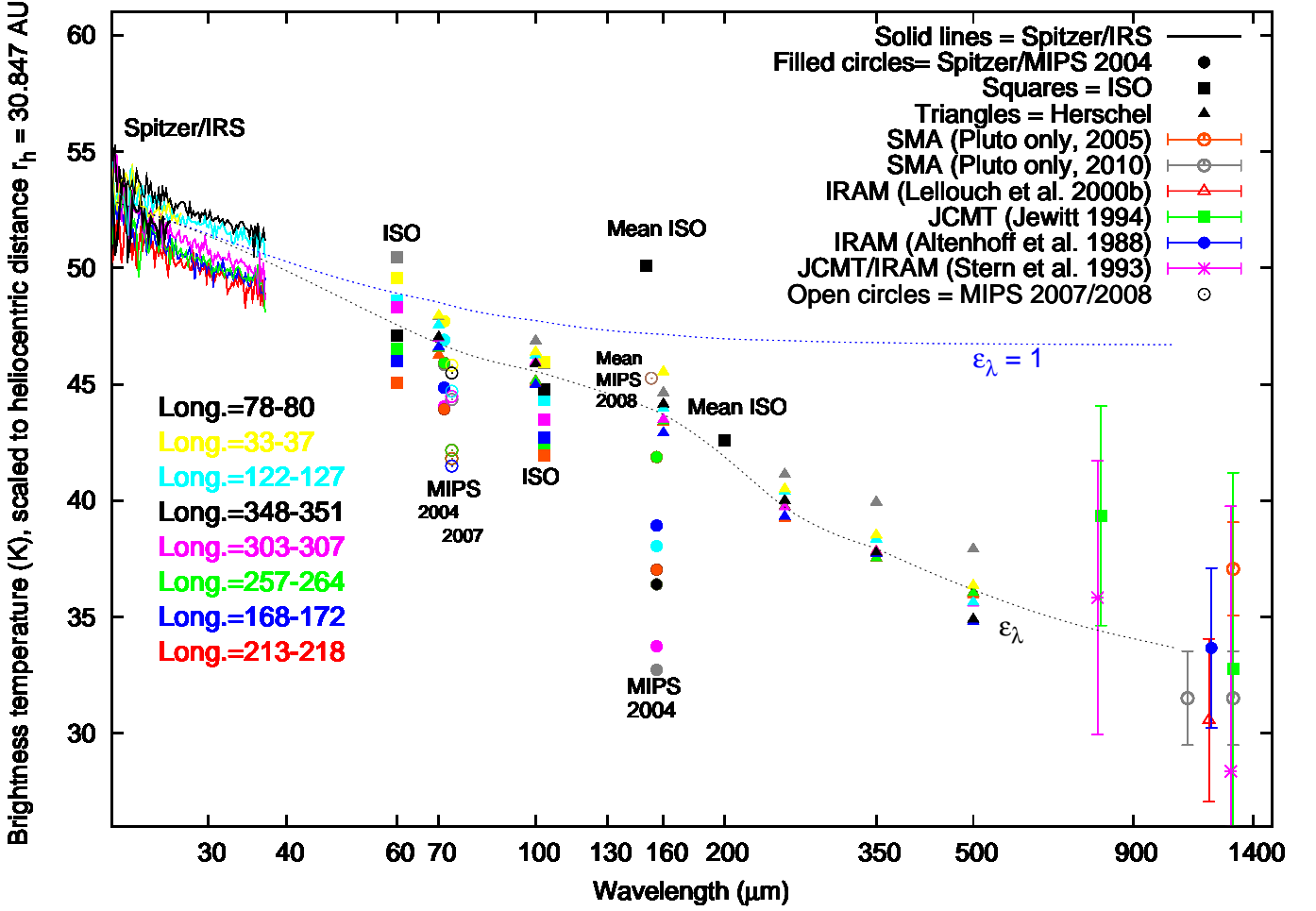


Fig. 2. Brightness temperature (T_B) of the Pluto system. Most thermal observations from ISO, *Spitzer*, *Herschel*, and ground-based telescopes are gathered. As data were acquired at different epochs spanning ~ 25 years, the T_B are rescaled by $1/\sqrt{r_h}$ to a common epoch (September 2004, $r_h = 30.847$ AU). Solid lines: eight *Spitzer*/IRS spectra over 21–37 μm , taken in Aug.–Sept. 2004 at east longitudes of 33 (yellow), 78 (gray), 122 (light blue), 168 (dark blue), 213 (red), 257 (green), 302 (pink), and 348 (black). Filled circles: *Spitzer*/MIPS photometric measurements, taken at similar longitudes (37, 80, 127, 172, 218, 264, 307, and 351, same color codes) in September 2004. The *Spitzer* data are taken from Lellouch et al. (2011) (Paper I). Open circles: additional *Spitzer*/MIPS data at 71.42 μm from April 2007 (see Fig. 13 from Paper I). Triangles: *Herschel* data at 70, 100, 160, 250, 250, and 500 μm from this work. Filled squares: data from ISO at 60 and 100 μm taken in 1997 (Lellouch et al., 2000a). The *Herschel*, *Spitzer* 2007 and ISO data are reinterpolated to the eight longitudes observed by *Spitzer* in 2004. The ISO 100 μm (resp. *Spitzer* 2007) data are shifted by 3 μm (resp. 2 μm) for easier legibility. The comparison between the open and filled circles at 71 μm illustrates the “Pluto fading” witnessed by *Spitzer* from 2004 to 2007. Additional data (averaged over longitudes, no error bar) from ISO at 150 and 200 μm , and from unpublished *Spitzer* 156 μm observations taken in October 2008, are shown as filled squares and open circles respectively, under the labels “Mean ISO” and “Mean MIPS 2008”. For ground-based datasets sampling more than one longitude, only the average T_B is plotted. The SMA-measured T_B refers to Pluto only. The dotted lines show thermophysical model fits (see text), calculated for the conditions of September 2004. Gray dotted line: parameters are from Case 4 in Table 2. Blue dotted line: same, but with spectral emissivities = 1. This latter case still produces brightness temperatures that decrease with wavelength, a consequence of the spatial mixing of different surface temperatures.

2004 data. (ii) The 150–160 μm T_B show large dispersion. While the original ISO–150 μm data (Lellouch et al., 2000a) indicated anomalously high fluxes ($T \geq 50$ K in average), the *Spitzer*/MIPS 156 μm data from April 2004 instead pointed to $T_B < 40$ K. The additional *Spitzer*/MIPS 156 μm unpublished data from October 2008 (12 visits) indicate a mean (rescaled) value of 45.3 K with a formal error of 1 K, but a 5.2 K dispersion over the 12 visits, which is a more likely representation of actual uncertainty. This mean value is generally in line, albeit somewhat on the higher side, with the 160 μm T_B indicated by *Herschel*. (iii) The ensemble of data clearly outlines the decrease of the system brightness

temperature with wavelength over the entire thermal range ($\lambda > 20$ μm). Although data in the sub-mm/mm range show large dispersion, the most accurate of them (i.e., the SMA data from 2010 (Gurwell, Butler & Moullet, 2011) and the IRAM Feb.–Mar. 2000 data from Lellouch et al. (2000b)) point to a ~ 32 K brightness temperature at 1100–1300 μm , i.e., a consistent “extrapolation” of the trend indicated by the *Herschel* data into the mm range. Thus it appears that the Pluto–Charon T_B decreases by more than 30 % of its value from 20 μm (~ 53 K) to 500 μm (~ 35 K) and beyond.

4.2. Emissivity

Qualitatively, a decreasing T_B with increasing wavelength can be produced in several ways: (i) a spatially constant surface temperature T and a low (but spectrally constant) surface emissivity; (ii) the mixing of different surface temperatures. Such a mixing can occur both on regional scales (e.g., different Pluto and Charon regions have different temperatures because of different albedos or because they see different instantaneous insulations) and on small scales (slopes at any scales, i.e., surface roughness, cause adjacent surface facets to see large variations of temperatures due to shadows and/or re-radiation); and (iii) a decrease of the spectral emissivity with wavelength. Scenario (i) is technically possible, but fitting the *Herschel*-measured brightness temperatures over 70-500 μm would require a constant $T \sim 52.5$ K and an improbably low (~ 0.57) spectrally constant surface emissivity. Rather, given the observed albedo variegation on Pluto and Charon, scenario (ii) must occur, at least on geographic scales. Based on multiterrain modeling of the *Spitzer* data, however, Paper I found that a decrease of the spectral emissivity with wavelength, i.e. scenario (iii), of some of the Pluto areas (the CH_4 ice regions) was also required.

Spectral “emissivity” is often loosely defined in the literature, and sometimes treated as a fudge factor in models. In essence, it represents the ratio of the observed fluxes to model fluxes, but how much physics is put into the models leads to different estimates of the “emissivity”. In early works, surface temperatures were described in simplistic end-member cases, such as the “nonrotating” or the “rapid rotator” cases. The advent of more elaborate models, such as the asteroid STM (Lebofsky et al., 1986) and NEATM (Harris, 1998), and of physically-based, thermophysical models (TPM; e.g., Spencer et al., 1989; Lagerros, 1996; Müller & Lagerros, 1998), provided a more realistic description of the surface temperature distribution across airless bodies, and thereby a definition of spectral emissivity in reference to fluxes emitted from the *surface*. However, a further complication is that, particularly at long wavelengths, the surface materials’ partial transparency may cause the emitted radiation not to originate at the surface itself, but from some characteristic depth that depends on the material absorption coefficient. Therefore, the emitted flux does not just depend on the surface temperature, but on the thermal profiles $T(z)$ within the subsurface. Consideration of this aspect leads to another definition of the emissivity, as the ratio of the observed to the modeled fluxes. The modeled flux, Φ_ν , at some frequency ν , is expressed locally as, e.g., (Keihm et al., 2013)

$$\Phi_\nu = \int B_\nu(T(z)) \exp\left(-\frac{z}{L_e \cos \mu}\right) \frac{dz}{L_e \cos \mu} \quad (1)$$

and spatially integrated over the object. Here B_ν is the Planck function, L_e is the electrical skin depth (inverse of the absorption coefficient), and μ is the viewing geometry dependent angle between the outgoing radiation and the surface normal.

Many asteroid studies (e.g., Redman, Feldman & Matthews, 1998; Müller & Lagerros, 1998), making use of *surface* temperature for reference, reported evidence for very low spectral emissivities (0.6-0.7) in the mm/sub-mm ranges, which were attributed to grain size dependent subsurface scattering processes. However, the recent comprehensive study by Keihm et al. (2013) demonstrated that when allowance is made for subsurface sounding (and for the enhancement of the infrared fluxes by surface roughness), the observed mm/sub-mm fluxes are generally consistent with spectral emissivities close to 1 (e.g., 0.95). This suggests that no scattering losses occur, except for specular re-

flexion at the surface, which can be characterized by a Fresnel coefficient with moderate (~ 2.3) dielectric constant, characteristic of low-density material. As discussed below, however, there are other planetary surfaces where thermal scattering effects are demonstrated to occur.

In our previous works (Lellouch et al., 2000a, 2011), the emissivity required to match the observed ISO or *Spitzer* fluxes was defined in reference to a thermophysical model that only considered the surface temperatures. A complication was related to the multiplicity of surface terrains. Three units (N_2 ice, CH_4 ice, tholin/ H_2O ice) were considered for Pluto and one for Charon, and the approach was to (i) fix the spectral and bolometric emissivity of all units except CH_4 and (ii) adjust them for the CH_4 unit, using for initial guidance expectations based on spectral properties of ices (Stansberry, Pisano & Yelle, 1996). Results (Paper I) suggested a large decrease of the spectral emissivity of CH_4 ice, from ~ 1 at 24 μm to ~ 0.4 at 200 μm . However, possible subsurface sounding effects were not considered, except in Lellouch et al. (2000b), where the nondetection of the 1.2 mm light curve was interpreted in terms of the mm-emissivity of the tholin/ H_2O ice unit. Furthermore, all of our previous thermophysical models were “diurnal-only”, i.e., they assumed equilibrium of the diurnally averaged temperatures with the instantaneous seasonal insolation. Thermal inertia effects on seasonal timescales are thought to be important in controlling the surface-atmosphere exchanges (Young, 2012, 2013; Olkin et al., 2015; Hansen, Paige & Young, 2015) and the atmospheric pressure. They may be important to include for our purposes because they are likely to impact the near-surface temperatures.

Along with the decreasing brightness temperatures with increasing wavelength, a striking result of the *Herschel* measurement is the low T_B value (~ 35 K) at 500 μm . Below we demonstrate that such a T_B is lower than any expected value for the dayside surface or subsurface of these bodies; thus, subsurface sounding toward the longest wavelengths is not the only cause of the decreasing T_B , so that “true” emissivity effects (as defined per Equation (1)) must occur.

4.3. Thermal modeling

One complication associated with modeling of long-wavelength thermal data is related to the unknown level probed by the emission within the surface, compared to the depth over which temperature changes occur (the thermal skin depth). Unlike in the thermal IR (e.g., 10-50 μm), where radiation is emitted from the surface itself (within a fraction of a mm), materials can be transparent enough in the sub-mm that thermal radiation might originate from layers ~ 10 to several thousand times the wavelength (i.e., 5 mm to 1 m or more at 500 μm). The thermal skin depth is related to the thermal inertia Γ through $d_s = \frac{\Gamma}{\rho c} \sqrt{\frac{P}{\pi}}$, where ρ is density, c is heat capacity, and P is the (diurnal or orbital) period. The parameter d_s is therefore not completely defined by Γ since ρ and c may not be well known². Still, using typical numbers for ρ (900 kg m^{-3}) and c (400 $\text{J kg}^{-1} \text{K}^{-1}$), a thermal inertia $\Gamma = 25 \text{ J m}^{-2} \text{ s}^{-0.5} \text{ K}^{-1}$ (hereafter MKS) for Pluto leads to a diurnal skin depth of 3 cm, meaning that sub-mm radiation could either probe within or below the diurnal skin depth and conceivably could even encompass a substantial fraction of the seasonal

² It can be shown (see, e.g., Le Gall et al. (2014) and Schloerb et al. (2015) for recent applications) that the outgoing thermal radiation depends on the ratio of the electric skin depth L_e to the relevant thermal skin depth, rather than on their absolute values.

skin depth (3.5 m for $\Gamma = 25$ MKS). A much larger thermal inertia ($\Gamma = 1000$ –3000 MKS) could be more appropriate on seasonal timescales (Olkin et al., 2015), however; then the seasonal skin depth would extend several hundreds of meters deep.

Given these uncertainties, our initial approach is to consider a number of situations of relative electrical, diurnal, and seasonal skin depths. For that we first model horizontal and vertical temperatures of a “mean” Pluto using a standard spherical thermophysical model (Spencer et al., 1989)³. By “mean Pluto”, we mean that we use a Bond albedo of 0.46 derived from a mean geometric albedo $p_V = 0.58$ and a plausible phase integral $q = 0.8$ (Lellouch et al., 2000a; Brucker et al., 2009). A bolometric emissivity of 1.0 is assumed and no surface roughness effects are included. As discussed below, the model is not relevant to the N_2 -ice covered areas whose heat budget is affected by sublimation/condensation terms.

4.3.1. Diurnal-only models

As a first step, we consider a “diurnal-only” model. In this case, the local insolation is calculated using “fixed” heliocentric distance and subsolar latitude relevant to early March 2012, which leads in particular to zero temperatures in the polar night southward of $43^\circ S$ ⁴. A thermal inertia of 25 MKS is assumed, following results from Paper I. Fig. 3 shows the resulting (i) surface temperatures and (ii) “subdiurnal” temperatures, i.e., temperatures at depths much below the diurnal skin depth, in both cases as seen from the observer (neglecting the small 1.6° phase angle). Surface temperatures (relevant to dayside) peak near ~ 56 K at high northern latitudes and fall below 35 K at latitudes below $20^\circ S$ only. Subdiurnal temperatures, which follow lines of equal latitude, are slightly colder than the surface temperatures by 0–5 K (except in the 6–10 am morning hours where they can be warmer than surface temperatures by up to 4 K). Planck-averaged disk surface (resp. subdiurnal) temperatures over 70 – $500 \mu m$ are 51.4 – 49.0 K (resp. 49.8 – 47.0 K). All these temperatures are comfortably higher than the mean $T_B \sim 35$ K measured by *Herschel*-SPIRE at $500 \mu m$, indicating that subsurface sound-ing within the diurnal layer is not the main culprit for this low T_B . Consideration of a possible positive thermal inertia gradient with depth in the diurnal layer would not change this conclusion because the subdiurnal temperature is an increasing function of thermal inertia (e.g., Fig. 2 of Spencer et al., 1989).

4.3.2. Seasonal models

The above approach does not consider the impact of thermal inertia on seasonal timescales. Continuing with a Bond albedo of 0.46 and bolometric emissivity $\epsilon_b = 1$, we show in Fig. 4 the seasonal temperature fields for two different values of the thermal inertia, $\Gamma = 25$ MKS and 3162 MKS. The first value, equal to that considered above for diurnal-only models, represents the situation of no thermal inertia gradient with depth. The second value represents one of the high thermal inertia cases favored by some of the recent climate models (Young, 2012, 2013; Olkin et al., 2015). In Fig. 4, the left panels show the 2-D (time, season) diurnally averaged (i.e., subdiurnal) surface temperatures; the right panels, which pertain to the epoch of the *Herschel* observations, show the latitudinal profile of: (i) this diurnally averaged tem-

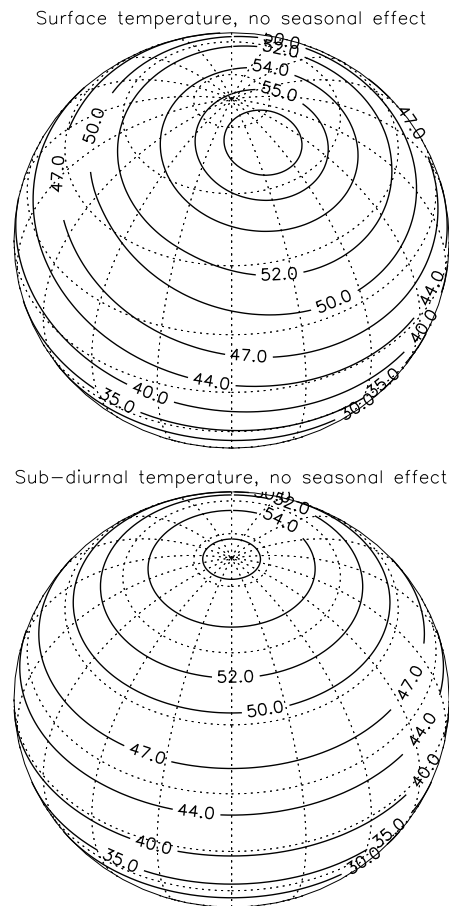


Fig. 3. Apparent Pluto temperatures, as viewed by a near-Sun observer in 2012, for a diurnal-only model with thermal inertia $\Gamma = 25$ MKS, Bond albedo = 0.46 and bolometric emissivity $\epsilon_b = 1$. *Top*: Surface temperatures. *Bottom*: Temperatures at the bottom of the diurnal layer.

perature; (ii) the “deep” temperature (i.e., the temperature much below the seasonal skin depth); and (iii) the minimum value in the seasonal temperature vertical profile at each latitude. For the low thermal inertia ($\Gamma = 25$ MKS) case, seasonal effects on the diurnally averaged surface temperature are small. The temperature profile shown in the top right panel of Fig. 4 closely matches the subdiurnal temperature map of Fig. 3, except near and within the polar night where the zero temperatures of the diurnal-only model are replaced by more physical ~ 20 K– 30 K values. In contrast, this model leads to rather cold temperatures of 30–36 K in the “deep” (i.e., subseasonal) subsurface, with minimum temperatures in the seasonal layer occasionally falling below 30 K at high northern latitudes.

The high ($\Gamma = 3162$ MKS) thermal inertia case⁵ has a much more dramatic effect on the diurnally averaged surface temperatures, which now show strongly subdued latitudinal contrasts of ~ 3 K for south pole to north pole at the *Herschel* epoch. In this situation, the deep temperatures reflect the mean insolation over the entire orbit and are almost hemispherically symmetric with maxima at the poles, minima near $\pm 30^\circ$ latitude, and a secondary

³ <https://www.boulder.swri.edu/~spencer/thermprojrs/>

⁴ This ignores internal heating. A typical radiogenic heating of $2.4 \text{ erg cm}^{-2}\text{s}^{-1}$ (Robuchon & Nimmo, 2011) would yield a ~ 14 K polar night temperature for unit bolometric emissivity.

⁵ The choice of 3162 MKS in Young (2013) and Olkin et al. (2015) is just an effect of their thermal inertia grid, with two values per decade, for parameter searches. No physical inference should be drawn from the fact that 3162 MKS is higher than the thermal inertia for solid H_2O at 40 K (2200 MKS, Spencer & Moore, 1992).

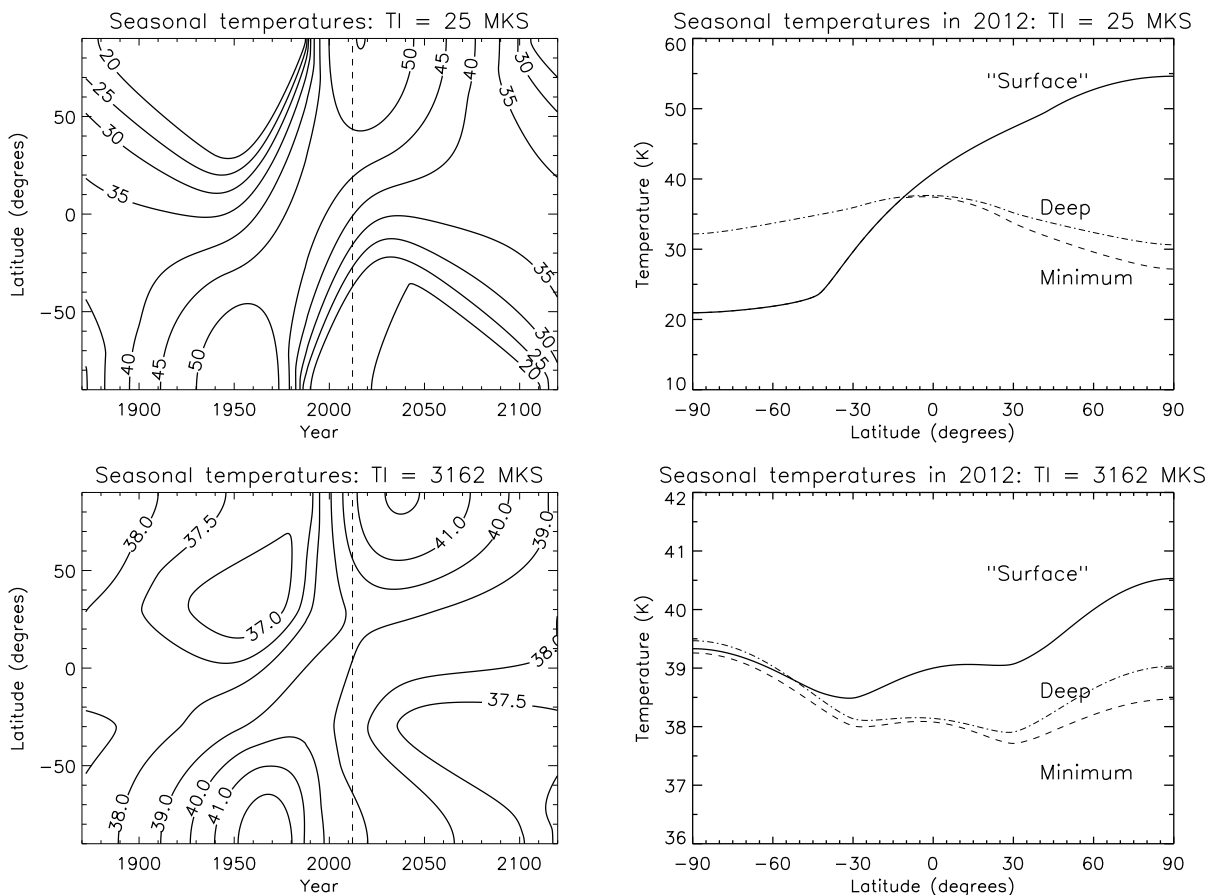


Fig. 4. Pluto temperatures from a seasonal model with thermal inertias $\Gamma = 25$ MKS (top) and 3162 MKS (bottom). A Bond albedo of 0.46 and bolometric emissivity $\epsilon_b = 1$ are used. *Left:* “Surface” temperature fields over a Pluto orbit. The dashed line indicates the epoch of the *Herschel* observations. *Right:* Temperatures as a function of latitude for early March 2012. “Surface” and “deep” indicate temperatures at the top and bottom of the seasonal layer. “Minimum” refers to the minimum temperature within the seasonal layer for each latitude.

maximum near the equator. These deep temperatures are in the range 38 K–39.5 K, and the minimum vertical temperature never falls below 37 K.

4.3.3. Comments and implications for the origin of low brightness temperatures

The temperatures shown in Fig. 3 and 4 are likely to be lower limits to the temperatures relevant to the *Herschel* observations for a number of reasons. First, they were calculated for a bolometric emissivity of 1.0, which, if anything, minimizes the calculated temperatures. Second, the geometric albedo that has been used is the Pluto-average value. Because the brightest regions are typically associated with N_2 ice, the non- N_2 ice regions are darker and thus warmer than the calculation indicates. Third, the above calculations do not include any increase of the effective emitting temperature due to roughness (those effects were incorporated in the form of a “thermophysical model beaming factor” in Lellouch et al., 2000a, 2011). Finally, while the *Herschel* beam encompasses Pluto and Charon, the above calculations pertain to Pluto only. Charon, which is slightly darker than Pluto, and based on the *Spitzer* 24 μm data likely to have a slightly smaller thermal inertia in the diurnal layer (Paper I), should therefore be warmer than Pluto on its dayside. This argument cannot be applied to the seasonal models however, as

the relative seasonal thermal inertias of Pluto and Charon are unknown.

Yet, the temperatures shown in Fig. 3 and 4 are only relevant to the Pluto units not covered by N_2 ice. The heat budget of the latter is dominated by sublimation-condensation exchanges, which, at a given point in time, maintain N_2 to an isothermal state over the globe and the surface pressure to an essentially constant value (except for topographic effects) that is buffered by the N_2 ice temperature (Young, 2012). The most recent volatile transport models (Young, 2012, 2013; Olkin et al., 2015; Hansen, Paige & Young, 2015) indicate N_2 ice temperatures constantly above 34 K throughout a Pluto year according to Hansen, Paige & Young (2015), and in the range 37.5–39.5 K according to Olkin et al. (2015), with $T(N_2) \sim 38.5$ K in 2012. The surface pressure determination from New Horizons is ~ 10 μbar in July 2015 (Stern et al., 2015), corresponding to equilibrium at 37.0 K (Fray & Schmitt, 2009). Because N_2 is horizontally isothermal (i.e., does not show any diurnal temperature variation), it must also be vertically isothermal, at least over the diurnal skin depth. A firm lower limit of the N_2 temperature is provided by the shape of the (2–0) band at 2.15 μm , which clearly indicates that N_2 is in the β phase (Tryka et al., 1994), i.e., above the transition to cubic α phase at 35.6 K (Scott, 1976; Trafton, 2015). All of this suggests that regions covered with N_2 ice are

also warmer, albeit not necessarily by much, than the mean 500- μm T_B that we measure (35 K, Fig. 1).

The above considerations show that in most situations physical temperatures at the surface and in the subsurface of Pluto and Charon are considerably higher than the observed system brightness temperatures at 500 μm and beyond. The exception is the case of the subseasonal temperatures for the case of low seasonal thermal inertia (25 MKS, i.e., comparable to the diurnal seasonal thermal inertia), which can be as low as 27-36 K (Fig. 4). We conclude that the low observed T_B do not result from the temperature gradient (colder at depth on the dayside) in the diurnal layer, but could conceivably be due to long-wavelength radiation probing a significant portion of the seasonal layer. This situation would require that (i) the seasonal thermal inertia is small, i.e., there is no significant vertical gradient of the thermal inertia, and (ii) the surface material is transparent enough that thermal radiation probes several meters below the surface.

Estimates of Pluto's seasonal inertia have been obtained from climate models (Hansen & Paige, 1996; Young, 2013; Hansen, Paige & Young, 2015; Olkin et al., 2015) designed to match the atmospheric pressure evolution witnessed since 1988 and constraints on Pluto's albedo distribution based on HST measurements. In addition to thermal inertia, these models include free parameters, such as the albedos and bolometric emissivities of the N_2 frost and the involatile substrate, and the amount of volatile inventory. Once tuned to the pressure measurements, these models can also predict the orbit-long evolution of Pluto's atmosphere. The latest two models, published prior to the *New Horizons* encounter, which give different priorities on the constraints to fit, differ rather radically in their conclusions with contrasting best-fit solutions for the seasonal thermal inertia (10-42 MKS in Hansen, Paige & Young (2015) vs 1000-3162 MKS for Olkin et al. (2015)) and diverging conclusions as to the fate of the atmosphere in the upcoming decades. The analysis of *New Horizons* data, particularly polar night temperatures with REX, should ultimately sort out this issue, but for now, we regard the seasonal thermal inertia of Pluto as significantly underconstrained.

However, even if the seasonal thermal inertia is small (i.e., comparable to the thermal inertia in the diurnal layer), we believe that the sub-mm radiation does not probe a large fraction of the seasonal skin depth (estimated above to be 3.5 m for $\Gamma = 25$ MKS). This stems from our estimate of the absorption coefficients of ices present on Pluto surface, on which we now elaborate. For N_2 ice and CH_4 ice, Lellouch et al. (2000a) presented absorption coefficients over 30-300 μm based both on early laboratory data compiled by Stansberry, Pisano & Yelle (1996) and on new optical constants measurements. These measurements (see Fig. 8 of Lellouch et al. (2000a)) indicate typical absorption coefficients of $\sim 0.5 \text{ cm}^{-1}$ for N_2 ice and $\sim 1 \text{ cm}^{-1}$ for CH_4 ice, i.e., penetration depths of 2 cm and 1 cm, respectively, which is much shallower than the above value of the seasonal skin depth. The significance of these penetration depths is actually uncertain because the volatile ices might actually be restricted to an even thinner surface veneer.

H_2O ice on Pluto has long escaped spectroscopic detection, and based on initial *New Horizons* data appears to be exposed only in a number of specific locations, usually associated with red color, suggestive of water ice/tholin mix (Grundy et al., 2015; Cook et al., 2015). Nonetheless, water ice is likely to be ubiquitous in Pluto's near subsurface, given its cosmogonical abundance, Pluto's density, and its presence on Charon's sur-

face⁶. Absorption coefficients for pure water ice ($k_{\text{H}_2\text{O}}$) at sub-mm-to-cm wavelengths are discussed extensively by Mätzler (1998), who also provides several analytic formulations to estimate them as a function of frequency and temperature along with illustrative plots. We use the Mishima, Klug & Whalley (1983) formulation (see Appendix of Mätzler, 1998). Its applicability is normally restricted to temperatures above 100 K, but Fig. 2 of Mätzler (1998) indicates the trend with temperature. Absorption coefficients extrapolated to 50 K (estimated as half the values at 100 K) are shown in Fig. 5. At 500 μm , our best estimate is $k_{\text{H}_2\text{O}} = 0.25 \text{ cm}^{-1}$, comparable to the above values for CH_4 and N_2 ices. The corresponding penetration length is therefore comparable to the diurnal skin depth but remains negligible compared to the seasonal skin depth, even for seasonal $\Gamma = 25$ MKS. According to these calculations, the seasonal layer would be probed only at a wavelength of ~ 4 mm and beyond. We also remark that the expression from Mishima, Klug & Whalley (1983) would give a penetration depth of 56 m at 2.2 cm, which is an order of magnitude larger than indicated by the laboratory measurements of Paillou et al. (2008). In addition, small concentrations of impurities can dramatically reduce the microwave transparency of water ice (e.g., Chyba, Ostro, & Edwards (1998) and references therein). Therefore, the above calculations likely indicate upper limits to the actual penetration depth of radiation in a H_2O ice layer, from which we conclude that the seasonal layer is not reached at the *Herschel* wavelengths.

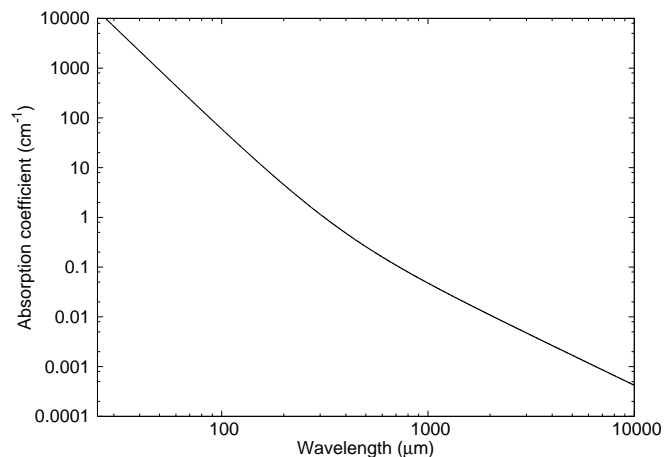


Fig. 5. Absorption coefficient of H_2O ice, extrapolated to 50 K (see text for details).

We conclude that the low brightness temperatures observed at the longest *Herschel* wavelengths cannot be explained by subsurface sounding, and imply emissivity effects. In what follows, we present models aimed at fitting the *Herschel* light curves to evaluate the mean spectral emissivity of the Pluto-Charon system.

4.4. Fit of Herschel data

Using the above thermophysical models, we expand upon the models developed previously for fitting the ISO and *Spitzer* data (Lellouch et al., 2000a, 2011). Briefly, these models described the Pluto-Charon system as composed of four units (N_2 ice, CH_4

⁶ Evidence for water ice bedrocks is also strongly suggested by the *New Horizons* discovery of several kilometer high topographic features on both Pluto's and Charon's surfaces (Stern et al., 2015).

ice, H₂O/tholin mix, and Charon), with specific distributions and geometric and bolometric albedos constrained by Pluto’s optical light curve, permitting one to calculate the thermal radiation (assumed Lambertian) of the entire system. The distribution of surface units was based on visible imaging and photometry (HST, mutual events) and near-infrared Earth-based spectroscopy. To calculate the local surface temperatures, a diurnal-only thermophysical model was used for all four units except N₂ ice, which was maintained at a fixed N₂ frost temperature. Another special condition was that the CH₄ temperature was allowed to vary in accordance to thermophysical model predictions, but was capped at a maximum 54 K temperature to account, in a simplified manner, for sublimation cooling effects for CH₄, which become important above this temperature (Stansberry et al., 1996b).

This “end-member” description is obviously outdated by the high-resolution *New Horizons*/LORRI imaging results (Stern et al., 2015), but until high-resolution maps of composition and albedo from LORRI and Ralph are available, it remains the only practical approach for our purpose. For now, we only considered the distribution favored in Paper I (“g₂”, their Fig. 4), remarking its rather nice consistency with the early LORRI/images (Fig. 6). Furthermore, this distribution is also roughly consistent with early compositional results from *New Horizons*/Ralph, which show both N₂ and CH₄ in Sputnik Planum, neither N₂ nor CH₄ in Cthulhu Regio, CH₄ north of Cthulhu and in the north polar region, and N₂ at mid-northern latitudes (Grundy et al. (2015), L. Young, priv. comm). The model free parameters are the thermal inertias of Pluto and Charon (expressed in terms of the thermal parameter Θ ⁷), plus the bolometric and/or spectral emissivity of some of the units, especially CH₄ ice. Fitting the *Spitzer* 2004 light curve makes it possible to estimate the thermal inertias of Pluto and Charon separately because the former primarily dictates the 24 μ m light-curve amplitude, while the latter determines the large contribution of Charon to the observed mean 24- μ m T_B (see Paper I for details).

We start by testing the best-fit model of Paper I determined from the *Spitzer* 2004 data. In this diurnal-only model, the spectral and bolometric emissivity of Charon and of the H₂O/tholin unit of Pluto were fixed to 1. Inferred parameters were the thermal parameters of Pluto and Charon, $\Theta_{PL} = 6$ (i.e., $\Gamma_{PL} = 22$ MKS) and $\Theta_{CH} = 4.5$ ($\Gamma_{CH} = 22$ MKS); bolometric emissivity of methane, $\epsilon_{b,CH_4} = 0.7$; and spectral emissivity of methane, $\epsilon_{CH_4} = 0.7, 0.6, \text{ and } 0.45$ at 70, 100, and 160 μ m, respectively. As indicated by the thin dotted lines in Fig. 7, this model (case 1 in Table 2), which provides an excellent fit of the *Spitzer* 2004 data, is inconsistent with the *Herschel* measurements as it yields brightness temperatures that are too low at 100 and 160 μ m, as well as too much light-curve contrast at these wavelengths. The first deficiency largely results from the poor quality of the *Spitzer* 2004 156 μ m measurements. These measurements, which are now shown to be inconsistent with other data (Fig.2), unduly skewed the model toward brightness temperatures that are too low. This deficiency can be corrected for by adjusting the CH₄ ice spectral emissivities (to 0.67, 0.80, 0.84, 0.58, 0.53, and 0.43 at 70, 100, 160, 250, 350, and 500 μ m, respectively; case 2 in Table 2). However the synthetic light curves (long dashed-lines in Fig. 7) still have too much contrast, except at 70 μ m.

⁷ Θ is related to the thermal inertia Γ by $\Theta = \frac{\Gamma \sqrt{\omega}}{\epsilon_b \sigma T_{SS}^3}$, where $\omega = 2\pi/(6.3872 \text{ days})$ is the body rotation rate, ϵ_b is the bolometric emissivity of the surface, σ is Stefan-Boltzmann’s constant, and T_{SS} is the instantaneous equilibrium temperature at the subsolar point,

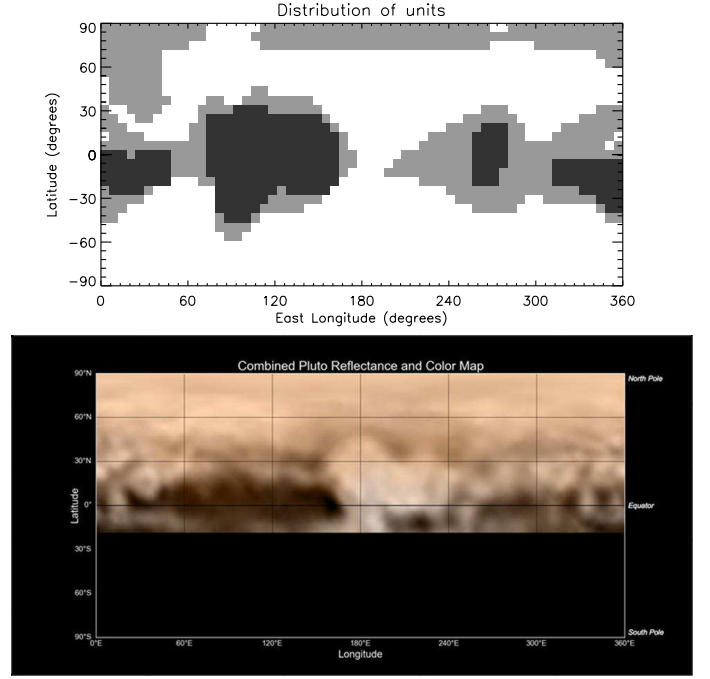


Fig. 6. Top: Adopted Pluto units for modeling (white = N₂, gray = CH₄, black = H₂O/tholin). Bottom: Map of Pluto created from images taken from June 27 to July 3 by the Long Range Reconnaissance Imager (LORRI) on *New Horizons*, combined with lower resolution color data from the spacecraft’s Ralph instrument. See <http://pluto.jhuapl.edu/Multimedia/Science-Photos/pics/nh-pluto-map.jpg>. Cthulhu Regio is the dark region covering $\sim 30^\circ\text{E}$ - 160°E longitudes. Sputnik Planum is the southern part of the bright region immediately to the east (informal names are taken from Stern et al., 2015).

This implies that the other units besides CH₄ ice are also subject to wavelength-dependent emissivities. Relaxing the hypothesis that the spectral emissivity of Charon and of the H₂O/tholin units are equal to unity, we searched for the spectral emissivity (now assumed for simplicity to be the same for Charon and the three Pluto units) that permits a fit to all light curves (case 3 in Table 2). This case permits a good fit (not shown in Fig. 7) to the data, but we do not regard it as satisfactory because the associated Planck-averaged bolometric emissivity is 0.82-0.85, which is inconsistent with the bolometric emissivities prescribed for the tholin/H₂O, CH₄ and Charon units (1.0, 0.7, and 1.0, respectively).

The above results point to the need to revise the *Spitzer*-derived models, and we here updated the fitting approach. For the sake of simplicity, we adopted fiducial bolometric emissivities of 0.90 for Charon and all Pluto units (for N₂ ice, the bolometric emissivity is not explicitly used; instead a uniform temperature is specified). We also do not include a “beaming factor” in the thermophysical model (as was done in Paper I), i.e., we ignore surface roughness effects; these are discussed separately later. With these changes to the model, the *Spitzer*-2004 24 μ m light curve was refit in terms of separate thermal parameters for Pluto and Charon at the *Spitzer* epoch, adopting a 24 μ m emissivity of 1.0 for all units. Best-fit $\Theta_{PL} = 7$ and $\Gamma_{CH} = 3$ values (i.e., $\Gamma_{PL} = 26$ MKS and $\Gamma_{CH} = 14$ MKS) were obtained. The thermophysical model was then re-run for the 2012 conditions, searching for the spectral emissivities (again assumed to be the same

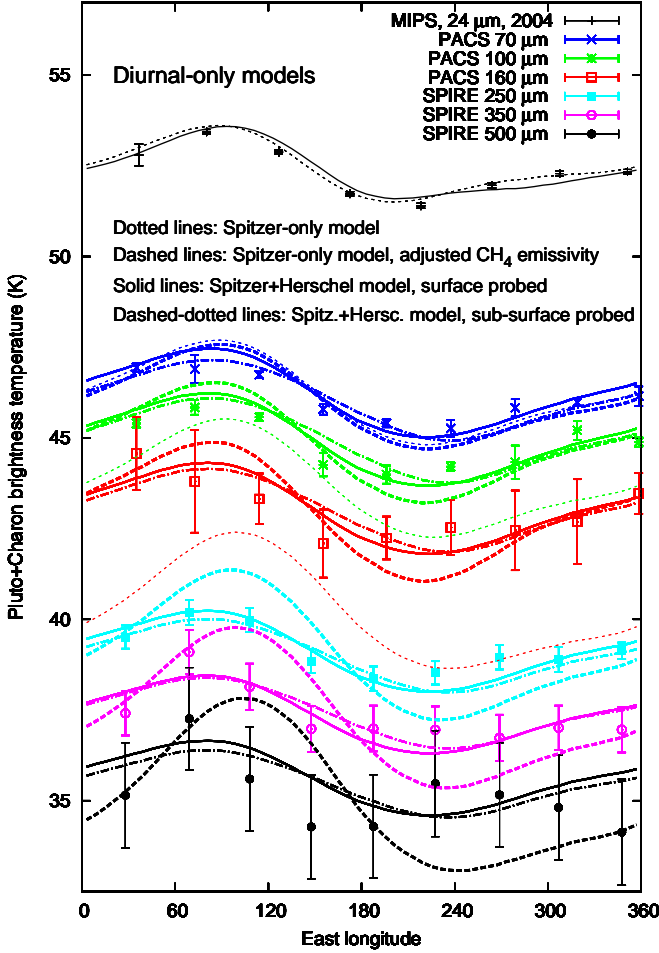


Fig. 7. Fits of the *Spitzer* 2004 (black points at top) and *Herschel* 2012 (all other points) brightness temperatures of the Pluto-Charon system using a diurnal-only model. Thin dotted lines: *Spitzer*-derived model (case 1 in Table 2). Dashed lines: *Spitzer*-derived model with CH_4 emissivities adjusted (case 2). Solid lines: New model (see text), assuming that radiation originates at the surface at all *Herschel* wavelengths (case 4). Dashed lines: Same, but assuming that radiation originates in the subdiurnal layer at all *Herschel* wavelengths (case 5).

for all units) that are permitted to fit the ensemble of *Herschel* light curves. Because there is considerable uncertainty in the penetration length of the far-IR radiation, we considered three cases: (i) small penetration at all six *Herschel* wavelengths, i.e., the surface itself is probed (case 4); (ii) large penetration, i.e., the subdiurnal layer is probed (case 5); and (iii) a wavelength-dependent absorption coefficient, following Fig. 5 (case 6). The required spectral emissivities for cases 4-6 are given in Table 2 and the associated emissivity curves are shown in Fig. 9. The overall fits of the thermal data for cases 4 and 6 are shown in Fig. 7 with solid and dashed-dotted lines, respectively.

Cases 4, 5, and 6 imply Planck-averaged bolometric emissivities of 0.83-0.86, 0.89-0.93, and 0.83-0.86. Although this is not precisely consistent with the adopted bolometric emissivities of 0.90, and although these models provide a somewhat worse fit to the $24\ \mu\text{m}$ data than do the “*Spitzer*-only” models, we consider that the overall solution is physically satisfactory, and that Fig. 9 provides a proper estimate of the spectral emissivity behavior of the Pluto-Charon system as a whole.

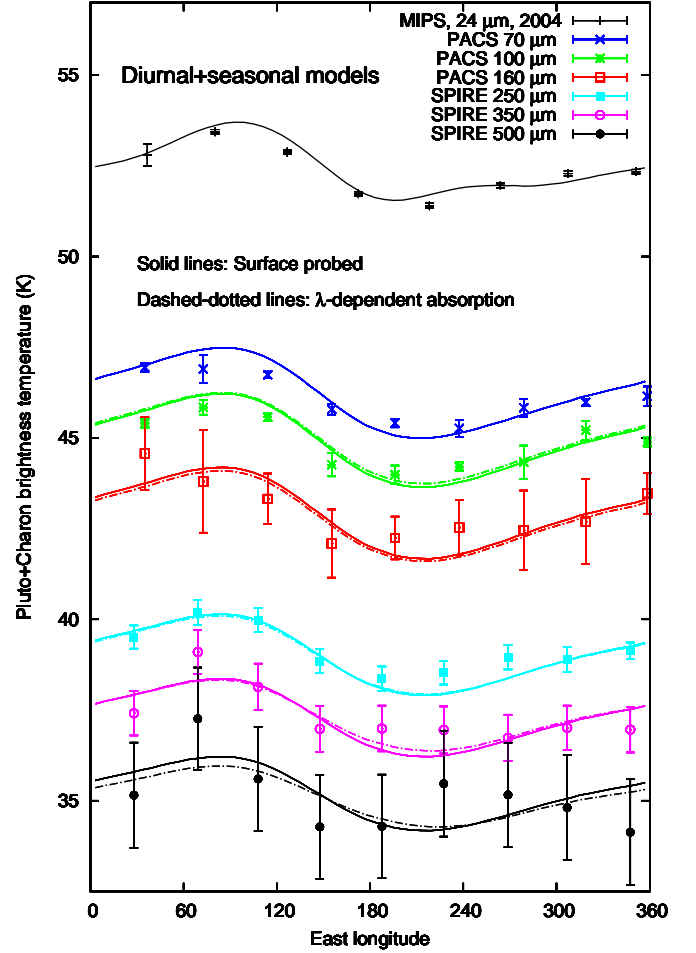


Fig. 8. Fits of the *Spitzer* 2004 (black points at top) and *Herschel* 2012 (all other points) brightness temperatures of the Pluto-Charon system using a seasonal+diurnal model. The seasonal thermal inertia is 2000 MKS. Solid lines: Model assuming that radiation originates at the surface at all *Herschel* wavelengths (case 4b in Table 2). Dashed lines: Same, but using the wavelength-dependent absorption coefficient from Fig.5 (case 6b).

The above results pertain to diurnal-only models. To study the effect of a large seasonal thermal inertia on the derived emissivities, cases 3 to 6 were reconsidered assuming that the subdiurnal temperature is determined by a seasonal thermal inertia of 2000 MKS (for both Pluto and Charon). Solution cases in terms of the diurnal thermal inertias and spectral emissivities are given in Table 2 (cases 3b to 6b). Since the large seasonal thermal inertia implies cold subdiurnal temperatures, somewhat smaller thermal inertias (compared to the diurnal-only case) are required to fit the *Spitzer* $24\ \mu\text{m}$ fluxes. Furthermore, these subdiurnal temperatures are in this case too cold (see also Fig. 4) to fit the *Herschel* 70, 100, and $160\ \mu\text{m}$ T_B , making this case (case 5b) not viable. In contrast, cases 3b, 4b, and 6b have emissivity solutions insignificantly different from corresponding cases 3, 4, and 6 (Table 2). Fits of the *Spitzer* $24\ \mu\text{m}$ and *Herschel* data with these seasonal + diurnal models (cases 4b and 6b) are shown in Fig. 8. They are almost indistinguishable from those shown in Fig. 7. Thus (and not surprisingly given that all our data pertain to nearly the same season), we are unable to constrain the seasonal thermal inertia from our data. Nonetheless, the ensemble

of model solutions (Table 2) yields diurnal thermal inertias $\Gamma_{PL} = 16\text{--}26$ MKS and $\Gamma_{CH} = 9\text{--}14$ MKS, confirming results from Paper I.

Model predictions for Case 4 of Table 2 over 20–1000 μm , calculated for the geometric conditions of September 2004 (subsolar latitude = 34.5°, heliocentric distance = 32.19 AU), are superimposed on Fig. 2 (gray dotted line). Although the figure gathers data with different subsolar latitudes, the fit shows the overall model adequacy. We do not attempt to fit the disparate set of sub-mm/mm data, noting that much improved constraints at these wavelengths are expected from ALMA (Butler et al., 2015). The same model, but in which spectral emissivities are forced to unity, is shown for comparison (blue dotted line). This latter case still shows a decrease of the brightness temperatures with wavelength as a result of the mixing of different surface temperatures (see Section 4.2), but this effect is clearly not sufficient to explain the data.

In a recent study, Trafton (2015) questioned the paradigm interpretation of Pluto’s near-infrared spectrum in terms of “pure” and “diluted” CH_4 ice, and, on thermodynamical grounds, proposed an alternate surface scenario with the mixture of areas covered by N_2 -rich ($\text{N}_2:\text{CH}_4$, saturated with CH_4) and CH_4 -rich ($\text{CH}_4:\text{N}_2$, saturated with N_2) solid solutions. For each unit, saturation of the secondary component occurs at the several percent level (about 3 % at 37 K; see Table 1 of Trafton, 2015). The $\text{CH}_4:\text{N}_2$ unit would correspond optically to what has been reported as “pure CH_4 ”, but with the key difference that this $\text{CH}_4:\text{N}_2$ unit would be isothermal because of the role of the N_2 -rich ice in transporting latent heat between solid solutions. As suggested by Trafton, thermal measurements may provide a test of these ideas. Coming back to the diurnal-only model (case 4 in Table 2) we attempted to remodel the *Spitzer* 24 μm light curve (best suited for this task because of its enhanced sensitivity to temperatures) under the assumption that the “ CH_4 ice unit” is actually isothermal at some constant temperature T_{CH_4} . As can be seen in Fig. 12 of Lellouch et al. (2011), the contribution of the CH_4 unit is most important over $L = 280\text{--}30$ (and responsible for the increase of flux with increasing longitude in this range). If the other components (Charon and tholin/ H_2O mix) are left untouched, the range of brightness temperatures measured in this longitude bin requires $T_{\text{CH}_4} = 51\text{--}52$ K, though the fit is not as good as it is with variable temperatures. Allowing for an increase in the contribution of the tholin/ H_2O or Charon unit (i.e., decreasing their thermal inertia) makes room for slightly lower values of T_{CH_4} (~ 50 K), but the shape of the calculated light curve degrades unacceptably below this temperature. We conclude that the 24 μm light curve measured by *Spitzer* (i) implies that if the “ CH_4 ice unit” actually represents isothermal CH_4 -rich $\text{CH}_4:\text{N}_2$ mixtures, these must be at least 50 K warm, i.e., much warmer than the N_2 -rich areas (~ 37 K); and (ii) favors spatially and diurnally variable temperatures for the CH_4 -dominated areas over the isothermal case. At face value, these conclusions do not support Trafton’s (2015) scenario of isothermal $\text{CH}_4:\text{N}_2$ at the same temperature as $\text{N}_2:\text{CH}_4$, although reconciliation might be possible if regions attributed to pure CH_4 actually represent a spotty coverage of $\text{CH}_4:\text{N}_2$ solutions at 37 K with nonvolatile material. Finally, at 50 K, the saturated N_2 abundance in $\text{CH}_4:\text{N}_2$ would be 2–3 times larger than at 37 K.

5. Discussion

5.1. Roughness effects?

The emissivities derived in this work (Table 2, Fig. 9) either make use of a simple treatment of surface roughness in the case of the “*Spitzer*-only” models (cases 2 and 3 in Table 2) or ignore roughness (cases 4, 5, 6, 4b, 6b). As reviewed, e.g., in Keihm et al. (2013) and Delbo et al. (2015), disk-integrated infrared measurements of airless bodies have long indicated flux enhancements in near zero-phase angle observations relative to thermophysical models of smooth surfaces (even if zero thermal inertia is used in these models). These flux enhancements, strongest at shorter thermal wavelengths, are commonly viewed as the effect of small-scale surface roughness. The latter results in a multiplicity of surface temperatures at any scale with an enhanced contribution of the hottest temperatures to the flux, particularly at shorter wavelengths. These effects led to the introduction of the “beaming factor” in the literature (e.g., Lebofsky et al., 1986; Harris, 1998; Delbo et al., 2015), whereby a semiempirical correction to the thermophysically calculated surface temperatures can be applied to match the infrared fluxes. While this approach is usually appropriate for fitting disk-averaged observations in terms of an object’s diameter and albedo, it becomes insufficient when dealing with multiwavelength, multiphase angle, and/or multi local-time data. Examples of its shortcomings have been demonstrated, for example, by comparing its predictions of center-to-limb temperature profiles to those of physical roughness models constrained by lunar thermal emission profiles (Rozitis & Green, 2011). Other evidence of thermal emission enhancements not amenable to a single “beaming factor” was obtained from spectral images of comets 103P/Hartley 2 and 9P/Tempel 1 (Groussin et al., 2013) at thermal wavelengths. These data indicate color temperatures that are barely dependent on incidence angle i , vastly exceeding predictions from smooth surface models at large values of i . This is interpreted by the fact that thermal emission from a given region of a comet is dominated by facets that are oriented toward the Sun with a temperature that is mostly independent of the “smooth” incidence angle, but instead strongly dependent on local topography (slopes, projected shadows) on sub-km to sub-mm scales. In Groussin et al. (2013), these effects were modeled by replacing the Planck function $B(\lambda, T)$ by a product $\Lambda \times B(\lambda, T)$, where T is the color temperature and Λ (< 1) represents in essence the fraction of an observed region that undergoes the highest temperatures, as measured by T . The Λ parameter was found to decrease with increasing incidence angle, as expected for progressively larger effects of projected shadows.

In many asteroid thermal models, macroscopic roughness (e.g., occurring on scales larger than the thermal skin depth) is usually described by crater models, accounting for effects of partial shadowing, scattering of sunlight, mutual radiative heat exchanges within depressions, using different approximations and methods of coupling with heat conduction. Key parameters are the crater surface coverage and depth-to-diameter ratio, which combine to define the surface “rms slope”. For example, Lagerros (1998) found that high roughnesses (rms slope $\sim 35^\circ$) are required to mimic, in a flux-averaged sense, the standard beaming factor for asteroids. Based on the crater formulation from Hansen (1977), Keihm et al. (2013)’s calculations for a typical 0.15 albedo asteroid at 2.5 AU with low thermal inertia indicate that large roughnesses (50 % coverage of hemispherical craters) produce flux enhancements (over the smooth surface case) by ~ 9 % at 100 μm , but as much as ~ 40 % at 12 μm (see

Table 2. Emissivity models

Case	Θ_{Pl}^a	Θ_{CH}^a	Γ_{Pl}	Γ_{CH}	ϵ_b^b	$\epsilon_{70,100,160,250,350,500\mu m}^c$	Model type
1	6	4.5	22	22	1.0, 0.7, 1.0	CH ₄ : .7,.6,.45, N/A, N/A, N/A ^d	surface temp.
2	6	4.5	22	22	1.0, 0.7, 1.0	CH ₄ : .67,.80,.84,.58,.53,.43	surface temp.
3	6	4.5	22	22	1.0, 0.7, 1.0	all : .84,.85,.83,.74,.72,.68	surface temp.
4	7	3	26	14	0.9, 0.9, 0.9	all : .85,.86,.84,.74,.72,.70	surface temp.
5	7	3	26	14	0.9, 0.9, 0.9	all : .95,.94,.89,.77,.75,.72	sub-diurnal temp.
6	7	3	26	14	0.9, 0.9, 0.9	all : .85,.86,.84,.75,.735,.71	λ -dept. absorption
3b ^e	4.5	2.5	16	12	1.0, 0.7, 1.0	all: .84,.85,.825,.73,.715,.68	surface temp.
4b ^e	4.5	2	16	9	0.9, 0.9, 0.9	all : .87,.87,.84,.74,.72,.69	surface temp.
5b ^e	4.5	2	16	9	0.9, 0.9, 0.9	all : N/A,N/A,N/A,.91,.85,.80	sub-diurnal temp.
6b ^e	4.5	2	16	9	0.9, 0.9, 0.9	all : .87,.87,.84,.755,.74,.73	λ -dept. absorption

^a Thermal parameters at *Spitzer* 2004 epoch

^b Bolometric emissivities of tholin/H₂O, CH₄ and Charon

^c Spectral emissivities or either CH₄ only or all units

^d *Spitzer* model: spectral emissivities of CH₄ only defined at 70, 100, and 160 μm

^e Models with seasonal inertia $\Gamma = 2000$ MKS. N/A in case 5b indicates no solution

their Fig. 1)⁸ and even more at shorter wavelengths. These calculated flux enhancements can be applied to other objects by noting that they are unique functions of $\lambda \times T$ by virtue of the Planck function dependence. “Transposing” a 0.15 albedo asteroid at $r_h = 2.5$ AU (which has an instantaneous subsolar temperature of $T_{SS} = 246.0$ K for $\epsilon=0.9$) to Pluto ($A = 0.46$, $r_h = 32.2$ AU, giving $T_{SS} = 61.2$ K), means that for equal roughness the same flux enhancements would occur for Pluto over 48 μm –400 μm . Although the case described by Keihm et al. (2013) presumably represents an upper limit of any realistic roughness for Pluto, the above comparison might suggest that wavelength-dependent roughness effects may affect the *Spitzer*+*Herschel* fluxes at typical levels of a few tens of percent. While the enhancements due to roughness are wavelength-dependent when considered in flux, they in fact imply approximately constant increases in brightness temperatures. Specifically, when reference is made to a smooth equilibrium model (EQM), the above flux enhancements for the considered asteroid imply brightness temperatures increases of 14–15 K over 12–100 μm . Rescaling to the Pluto case would mean that the 48 μm –400 μm T_B could be affected by roughness effects at the 3–4 K level at most with essentially no spectral dependence⁹. This is a small fraction of the observed T_B decrease (~ 15 K) over that interval (Fig. 2). The potential 3–4 K effect is even dwarfed by the 10 K T_B difference associated with a spectral emissivity of ~ 0.7 , as we find required by the 500 μm T_B (Table 2). Finally and most importantly, and as alluded to in Section 4.3.3, since surface roughness can only enhance disk-averaged fluxes, any significant effects would actually exacerbate (by a few K) the fact, outlined in Section 4.3, that the long-wavelength T_B are below any plausible temperatures within Pluto’s subsurface. We are left to conclude that roughness effects are not the cause of the emissivity spectral dependence that we observe.

5.2. Comparison to other bodies and interpretation

Modeling of the *Herschel* data has led us to (i) an updated estimate of the Pluto and Charon diurnal thermal inertias, and (ii)

⁸ Similar numbers are obtained from the crater model of Müller (2002).

⁹ For comparison, the “thermophysical beaming factor” used in Paper I was 0.905–0.925, corresponding to a typical ~ 1 K increase of the brightness temperatures.

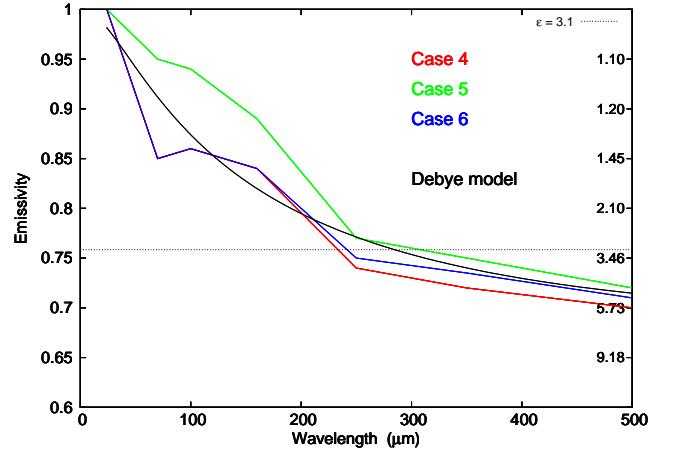


Fig. 9. Derived emissivities for models 4–6 (see text and Table 2). These emissivities are compared to predictions for a smooth surface with dielectric constants indicated on the right y scale (the dotted line is for a dielectric constant of 3.10) and for a Debye model with $\epsilon_s = 5$, $\epsilon_\infty = 1$ and $\nu_r = 10$ cm^{-1} (see text).

an assessment of their spectral emissivities over 20–500 μm . We determine $\Gamma_{PL} = 16$ –26 MKS and $\Gamma_{CH} = 9$ –14 MKS, in good agreement from inferences based on *Spitzer*-only data (Paper I), namely $\Gamma_{PL} = 20$ –30 MKS and $\Gamma_{CH} = 10$ –150 MKS (with most solutions calling for $\Gamma_{CH} = 10$ –20 MKS). These thermal inertias are low compared to those of compact ices, but still factors-of-several higher than the value statistically determined for the TNO population ($\Gamma = 2.5 \pm 0.5$ MKS, Lellouch et al., 2013b). As discussed in that paper, the difference does not necessarily imply intrinsically different thermal surface properties. For equal density and conduction properties, the diurnal skin depth at Pluto/Charon ($P = 6.387$ day) is ~ 5 times larger than that of a typical TNO with an 8-hour rotation period; hence the difference between Charon and a typical TNO might simply be consistent with an approximately linear increase of the thermal inertia with depth. The apparently higher thermal inertia at Pluto vs Charon may be related to atmospheric-assisted conduction in a porous surface (Lellouch et al., 2000a).

The very large ($>30\%$) decline of the Pluto-Charon brightness temperatures from ~ 20 to 500 μm , and probably beyond, is partly caused by the mixing of different temperatures on re-

gional scales. The main conclusion of our work is that, once this is taken into account, the remainder of the effect is not caused by surface roughness or subsurface sounding at the longest wavelengths, so that “genuine” emissivity spectral dependence occurs. This conclusion confirms and expands that reached for the 1.2 mm emission of the Pluto-Charon system (Lellouch et al., 2000b).

Low emissivities at long wavelengths have been observed on a number of solar system icy bodies. Muhleman & Berge (1991) reported 3-40 mm flux measurements of Europa and especially Ganymede indicating brightness temperatures well below the subdiurnal temperature, confirming earlier results from De Pater, Brown & Dickel (1984). Using Cassini/RADAR, Ostro et al. (2006) determined 2.2 cm brightness temperatures of several Saturn satellites. When comparing these brightness temperatures to the “isothermal equilibrium temperature” (i.e., the mean equilibrium surface temperature over a sphere), this implied averaged emissivities as low as 0.44 for Tethys, 0.59 for Enceladus and Rhea, and 0.69-0.81 for Iapetus. A 0.6-0.7 emissivity was also found at Enceladus by Ries & Janssen (2015). However, these estimates did not include the effect of subsurface sounding. Focusing on Iapetus, but using a thermophysical modeling including subsurface sounding, Le Gall et al. (2014) determined slightly higher emissivities (0.78-0.87, depending on the regions), but still significantly below unity. Also at Iapetus, Ries (2012) determined an extraordinarily low 9 mm effective emissivity (~ 0.3 - 0.4) on the trailing side. Emissivity effects are also seen in millimeter-wavelength measurements of various kinds of ice and snow on Earth (Hewison & English, 1999).

Fewer emissivity measurements are available in the far-IR (as opposed to sub-mm/cm wavelengths). From ISO/LWS observations of Mars, Burgdorf et al. (2000) inferred a spectral emissivity declining from 0.97 at 50 μm to 0.92 at 180 μm . Using *Herschel*, Leyrat et al. (2012) inferred a large decrease of the spectral emissivity of asteroid 4 Vesta, from 0.9 at 70 μm to 0.7 at 500 μm , essentially confirming previous findings by Müller & Lagerros (1998). These analyses, however, while including a detailed surface temperature model, did not account for possible subsurface sounding effects. Evidence for a spectrally-decreasing emissivity was also found for several Kuiper Belt and Centaurs by Fornasier et al. (2013) from combined *Spitzer*/MIPS, *Herschel*/PACS, and *Herschel*/SPIRE data. Although once again, this work did not explicitly include vertical temperature profiles, a striking observational fact was the abrupt fall-off of the emitted fluxes beyond 300 or 400 μm , with most objects not detected at 500 μm .

Our results for Pluto-Charon add further evidence that unlike dust/rock regolith asteroids (Keihm et al., 2013), icy solar system surfaces show long-wavelength emissivity effects not amenable to a combination of surface roughness and subsurface sounding. Reasons for lower-than-unity emissivities may include (i) dielectric constants larger than 1, implying reflection of the upward thermal radiation at the surface interface; (ii) particle scattering, which produces an emissivity minimum for particle sizes comparable to $\lambda/4\pi$; and (iii) volume scattering, whereby the combination of a weakly-absorbing medium down to the electrical skin depth and inhomogeneities or voids on scales comparable or larger than the wavelength causes internal reflections (Ostro et al., 2006; Le Gall et al., 2014). Volume scattering is commonly invoked as the dominant scattering mechanism at microwave (mm-cm) wavelengths (Janssen et al., 2009; Le Gall et al., 2014; Ries & Janssen, 2015).

In the measurements of Hewison & English (1999), the ice/snow emissivity dependence with frequency varies with the

age, wetness, surface state, and transparency of the ice as a result of the combination of dielectric and scattering effects. This was modeled in a semiempirical way using a Debye-like form of the complex permittivity,

$$\epsilon(\nu) = \frac{\epsilon_s - \epsilon_\infty}{1 - i\nu/\nu_r} + \epsilon_\infty$$

from which Fresnel coefficients can be calculated as a function of incidence angle. Here ϵ_s is the effective static permittivity, ϵ_∞ its high-frequency limit and ν_r is the effective relaxation frequency. This parameterization handles both dielectric surfaces (by setting $\epsilon_s > \epsilon_\infty$) and volume scattering ($\epsilon_s < \epsilon_\infty$), and both behaviors are found in terrestrial icy material. Adopting the above parameterization, and assuming a smooth surface and an equal mix of the two polarizations when calculating the Fresnel coefficients, the spectral dependence we derive for Pluto-Charon’s emissivity can be approximately fit with $\epsilon_s = 5$, $\epsilon_\infty = 1$, and $\nu_r = 10 \text{ cm}^{-1}$ (Fig. 9). The values of ϵ_s and ϵ_∞ encompass that of the water ice dielectric constant (3.10-3.13 at 50-100 K; Gough, 1972; Paillou et al., 2008), for which a ~ 0.76 constant spectral emissivity would be expected. Nonetheless, the above should be seen primarily as a working empirical model, and $\epsilon_s > \epsilon_\infty$ suggests that volume scattering may not be important in causing the depressed emissivities over 70-500 μm . In fact, as the volume scattering process operates in the electrical depth layer and for voids/inhomogeneities larger than the wavelength, it cannot be important when the absorption coefficient becomes smaller than the inverse of the wavelength, i.e., below 100 μm for H_2O ice.

The emissivity decrease with wavelength, possibly extending toward the mm range, may also indicate particle scattering with a typical particle size of at least 100 μm . Stansberry, Pisano & Yelle (1996) performed emissivity calculations for N_2 ice and CH_4 ice with various grain sizes, based on Hapke theory (Hapke, 1993) and their far-IR absorption properties. Their results do indicate significantly less than unity far-IR emissivities, but the spectral behavior, with an emissivity decrease occurring only longward of 50 μm for CH_4 and 150 μm for N_2 , is not consistent with the mean emissivity behavior we infer here. A similar problem was noted in Paper I, where the high 24 μm emissivity inferred for CH_4 ice was inconsistent with the calculations of Stansberry, Pisano & Yelle (1996) for a broad range of grain sizes. Calculations for H_2O ice are not available but the similarity of its absorption coefficient to that of N_2 and CH_4 ice at $\sim 300 \mu\text{m}$ (about 1 cm^{-1}) indicates that IR emissivities lower than unity are to be expected. Notwithstanding with the above issues, we conclude that the mean emissivity curve we have derived likely results from the combination of a high dielectric constant and particle scattering in relatively transparent surface ices.

The temperature of Pluto’s N_2 ice can be inferred from the atmospheric pressure. The buffering temperature of a 10 μbar N_2 atmosphere (Stern et al., 2015) is 37.0 K (Fray & Schmitt, 2009). An expression for the globally constant temperature of the N_2 ice (T_{N_2}) can be found in Stansberry & Yelle (1999) as a function of γ , the ratio of the total area of N_2 ice to its cross-sectional area as viewed from the Sun. For ubiquitous N_2 frosts (and many other reasonable surface ice configurations), $\gamma = 4$, and $T_{\text{N}_2} = T_{\text{SS}}/\sqrt{2}$. For $r_h = 32.9 \text{ AU}$ (July 2015), $T_{\text{N}_2} = 37.0 \text{ K}$ implies a relationship between the Bond albedo (A_b) and bolometric emissivity, namely $(1-A_b)/\epsilon_b = 0.335$. For the N_2 ice unit of the assumed terrain distribution (“g2”), Paper I derived a geometric albedo of 0.73, and assumed a phase integral of 0.90, yielding $A_b = 0.657$. With a bolometric emissivity $\epsilon_b =$

0.9 as we advocate here, this yields $(1-A_b) / \epsilon_b = 0.381$. The agreement with the above value is only approximate but could be brought to perfection with very small changes, e.g., using $\gamma = 4.5$ instead of 4 or a phase integral of 0.96 instead of 0.90. Furthermore, our nominal value of 0.381 matches well the range of solutions derived from the climate models (Young, 2013; Hansen, Paige & Young, 2015). Indeed, restricting the discussion to models that best approach a $\sim 10 \mu\text{bar}$ pressure in 2015 (cases PNV21-23 and EPP14 from Young (2013), and models #55 and #66 from Hansen, Paige & Young (2015)), these models all converge to $(1 - A_b) / \epsilon_b$ in the range 0.363–0.375. Thus, it appears that there is no major difficulty with a N_2 bolometric emissivity of 0.9. The heat budget for N_2 ice will be best revisited after results from photometric (albedos, phase integrals) investigations from *New Horizons* become available.

Although the *New Horizons* spacecraft does not carry a dedicated thermal radiometer, the Radio Experiment (REX) acquired measurements of the thermal emission from Pluto at 4.2 cm during two linear scans across the disk at close range including both day and night sides, and a third scan was obtained during the dark side transit of the occultation (Linscott et al., 2015). These data should provide crucial information on the surface temperature and its spatial variations, especially on the polar night temperature, which is the most diagnostic of thermal inertia on seasonal timescales (see Fig. 4). The present work suggests that emissivity effects will strongly impact the interpretation of these data.

The fits of the *Herschel* data presented here should still be viewed as preliminary. Future analyses making use of detailed surface maps based on *New Horizons*/Ralph (including albedo, composition and its vertical stratigraphy, particle size, phase functions, and possibly temperatures from band shape) will be possible when those datasets become available (e.g., Grundy et al., 2015). More generally, the ISO, *Spitzer*, and *Herschel* combined Pluto-Charon light curves constitute a legacy dataset at thermal wavelengths, against which temperature predictions from seasonal climate models should be tested, which will be soon complemented by additional data. Rotationally resolved ALMA data separating Pluto from Charon are already available (Butler et al., 2015), and thermal maps at $\sim 0.01''$ spatial resolution will be achievable in the coming years. Starting in 2018, the JWST/MIRI will measure Pluto and Charon emission over $\sim 10\text{--}27 \mu\text{m}$. These facilities will be invaluable to study the predicted evolution of the surface thermal properties as the Pluto system recedes from the Sun.

Acknowledgements. PACS has been developed by a consortium of institutes led by MPE (Germany) and including UVIE (Austria); KU Leuven, CSL, IMEC (Belgium); CEA, LAM (France); MPIA (Germany); INAF-IFSI/OAA/OAP/OAT, LENS, SISSA (Italy); IAC (Spain). This development has been supported by the funding agencies BMVIT (Austria), ESA-PRODEX (Belgium), CEA/CNES (France), DLR (Germany), ASI/INAF (Italy), and CICYT/MCYT (Spain). SPIRE has been developed by a consortium of institutes led by Cardiff University (UK) and including Univ. Lethbridge (Canada); NAOC (China); CEA, LAM (France); IFSI, Univ. Padua (Italy); IAC (Spain); Stockholm Observatory (Sweden); Imperial College London, RAL, UCL-MSSL, UKATC, Univ. Sussex (UK); and Caltech, JPL, NHSC, Univ. Colorado (USA). This development has been supported by national funding agencies: CSA (Canada); NAOC (China); CEA, CNES, CNRS (France); ASI (Italy); MCINN (Spain); SNSB (Sweden); STFC, UKSA (UK); and NASA (USA). Additional funding support for some instrument activities has been provided by ESA. Data presented in this paper were analyzed using “HIPE”, a joint development by the *Herschel* Science Ground Segment Consortium, consisting of ESA, the NASA *Herschel* Science Center, and the HIFI, PACS, and SPIRE consortia. We are indebted to the ESA staff, in particular Rosario Lorente and Mark Kidger, for a flexible and flawless implementation of the observations. E.L., S.F., and R.M. were supported by the French Programme National de Planétologie. C.K. and G.M. were supported by the OTKA/NKFIH K-104607 grant of the Hungarian

Research Fund / National Research, Development and Innovation Office; and the contract 4000109997/13/NL/KML of the Hungarian Space Office and the European Space Agency. Support for the work of S.P. was provided by NASA through an award issued by JPL/Caltech. We thank Leslie Young for constructive comments.

References

- Altenhoff, W. J., Chini, R., Hein, H., et al., 1988, A & A, 190, L15
 Brucker, M., Grundy, W.M., Stansberry, J., et al., 2009, Icarus, 201, 284
 Butler, B., Gurwell, M., Lellouch, E., et al., 2015, 47th DPS meeting.
 Burgdorf, M.J., Encrenaz, T., Lellouch, E., et al. 2000, Icarus, 145, 79
 Buie, M.W., Tholen, D.J., Wasserman, L.H., 1997, Icarus, 125, 233
 Chyba, C.F., Ostro, S.J., & Edwards, B., 1998, Icarus, 134, 292
 Cook, J.C., Cruikshank, D.P., Dalle Ore, C.M. et al., 2015, 47th DPS meeting.
 Delbo, M., Mueller, M., Emery, J.P., & al., 2015, Asteroid thermophysical modelling, Asteroids IV
 De Pater, I., Brown, R.A., & Dickel, J. R., 1984, Icarus 57, 93
 Fornasier, S., Lellouch, E., Müller, T., et al., 2013, A&A, 555, A15
 Fray, N., & Schmitt, B., 2009, Planet. Space Sci., 57, 2053
 Gough, S.R., 1972, Can. J. Chem. 50, 3046
 Griffin, M., Abergel, A., Abreu, A., et al., 2010, A&A, 518, L3
 Groussin, O., Sunshine, J.M., Feaga, L.M., 2013, Icarus, 222, 580
 Grundy, W.M., Buie, M.W., Stansberry, J.A., et al., 1999, Icarus, 142, 536
 Grundy, W.M., Schmitt, B., & Quirico, E., 2002, Icarus, 185, 486
 Grundy, W., et al., 2015, 47th DPS meeting.
 Gurwell, M.A., Butler, B., Moullet, A., 2011, EPSC-DPS Joint Meeting 271.
 Hansen, O.L., 1977, Icarus 31, 456
 Hansen, C.J., & Paige, D.A., 1996, Icarus, 120, 247
 Hansen, C.J., Paige, D.A., & Young, L.A., 2015, Icarus, 246, 183
 Hapke, B.W., 1993, Theory of reflectance and emittance spectroscopy, Cambridge Univ. Press, Cambridge
 Harris, A.W., 1998, Icarus, 131, 291
 Hewison, T.J., & English, S.J., 1999, IEEE Trans. Geosc. Remot. Sound., 37, 1871
 Janssen, M.A., Lorenz, R.D., West, R., et al., 2009, Icarus, 200, 222
 Jewitt, D.C., 1994, AJ, 107, 372
 Keilm, S., Kamp, L., Gulkis, S., 2013, Icarus, 226, 1186
 Kiss, Cs., Müller, T.G., Vilenius, E., et al., 2014, Exp. Astr., 37, 161
 Lagerros, J.S.V., 1996, A&A, 310, 1011
 Lagerros, J.S.V., 1996, A&A, 332, 1123
 Lebofsky, L.A., Sykes, M.V., Tedesco, E.F., et al., 1986, Icarus, 68, 239
 Le Gall, A., Leyrat, C., Janssen, M.A., et al., 2014, Icarus, 241, 221
 Lellouch, E., Laureijs, R., Schmitt, B., 2000a, Icarus, 147, 220
 Lellouch, E., 2000b, Icarus, 147, 580
 Lellouch, E., Stansberry, J., Emery, E., et al., 2011, Icarus, 214, 701 [Paper I]
 Lellouch, E., Santos-Sanz, P., Fornasier, S., et al., 2013, EPSC conference, #2013-91
 Lellouch, E., Santos-Sanz, P., Lacerda, P., et al., 2013, A&A, 557, A60
 Lellouch, E., de Bergh, C., Sicardy, B., et al., 2015, Icarus, 246, 268
 Leyrat, C., Barucci, A., Müller, T., et al. 2012, A & A, 539, 154
 Linscott, I., et al., 2015, 47th DPS meeting.
 Mätzler, C., 1998, In Solar System Ices (B. Schmitt, C. de Bergh, and M. Festou, Eds.), 241, Kluwer Academic
 Marton, G., Kiss, Cs., Balog, Z., et al., 2015, A&A, 579, L9
 Mishima, O., Klug, D.D., & Whalley, E., 1983, J. Chem. Phys., 78, 6399
 Muhleman, D.O., & Berge, G.L., 1991, Icarus, 92, 263
 Müller, T.G., 2002, Meteor. Planet. Sci., 2002, 37, 1919
 Müller, T.G., Lellouch, E., Stansberry, J., et al., 2010, A&A, 518, L146
 Müller, T.G., & Lagerros, J.S.V. 1998, A&A, 338, 340
 Nguyen, H.T., Schulz, B., Levenson, L., 2010, A&A, 518, L5
 Olkin, C.A., Young, L.A., Borncamp, D., et al., 2015, Icarus, 246, 220
 Ostro, S.J., West, R.D., Janssen, M.A., et al., 2006, Icarus, 183, 479
 Ott, S., 2010, ASPC, 434, 139
 Pailou, P., Lunine, J., Ruffié, G. et al., 2008, GRL, 35, 18
 Pilbratt, G., Riedinger, J.R., Passvogel, T. et al., 2010, A&A, 518, L1
 Poglitsch, A., Waelkens, C., Geis, N., et al., 2010, A&A, 518, L2
 PACS Photometer Point/Compact Source Mode 2010, PICC-ME-TN-036, <http://herschel.esac.esa.int/wiki/bin/view/Public/PacsCalibration>
 Quirico, E., & Schmitt, B., 1997, Icarus, 128, 181
 Redman, R.O., Feldman, P.A., & Matthews, H.E., 1998, AJ, 116, 1478
 Reuters, D.C., et al., 2008, Space Sci. Rev., 140, 129
 Ries, P., 2012, Ph.D. Thesis, University of Virginia
 Ries, P.A., & Janssen, M., 2015, Icarus, 257, 88
 Robuchon, X., & Nimmo, F., 2011, Icarus, 216, 426
 Rozitis, B., Green, S.F., 2011, MNRAS, 415, 2042
 Sicardy, B., Bellucci, A., Gendron, E. et al., 2006, Nature, 439, 52

- Santos-Sanz, P., Lellouch, E., Fornasier, S., et al., 2012, *A&A*, 541, A92
- Scott, T.A., 1976. Solid and liquid nitrogen. *Phys. Rep.*, 27, 87
- Schloerb, F.P., Keihm, S., von Allmen, P., et al., 2015, *A&A*, 583, A29
- Spencer, J.R., & Moore, J.M., 1992, *Icarus*, 99, 261
- Spencer, J.R., Lebofsky, L.A., & Sykes, M.V., 1989, *Icarus*, 78, 337
- Stansberry J.A., Pisano, D.J. & Yelle, R.V., 1996, *Planet. Space Sci.*, 44, 945
- Stansberry J.A., Spencer, J.R., Schmitt, B., et al., 1996, *Planet. Space Sci.*, 44, 1051
- Stansberry J.A., & Yelle, R.V., 1999, *Icarus*, 141, 239
- Stansberry, J., Grundy, W., Brown, M., et al. 2008, in *Physical Properties of Kuiper Belt and Centaur Objects: Constraints from the Spitzer Space Telescope*, eds. M.A. Barucci, H. Boehnhardt, D.P. Cruikshank and A. Morbidelli, 161
- Stern, S.A., Weintraub, D.A., & Festou, M.C., *Science*, 261, 1713
- Stern, S.A., Bagenal, F., Ennico, K., et al. 2015, *Science*, 350, 6258
- Trafton, L.M., 2015, *Icarus*, 246, 197
- Tryka, K.A., Brown, R.H., Cruikshank, D.P., et al. *Icarus*, 112, 509
- Tryka, K.A., Brown, R.H., Anicich, V., 1995, *Icarus*, 116, 409
- Young, L.A., *Icarus*, 221, 80
- Young, L.A., *AJ*, 766, L22.